3-2005

Boundary Layer Flow Control Using Plasma Induced Velocity

Brian E. Balcer

Boundary Layer Flow Control Using Plasma Induced Velocity

THESIS

Brian E. Balcer, 2Lt, USAF

AFIT/GAE/ENY/05-M03

DEPARTMENT OF THE AIR FORCE
AIR UNIVERSITY

AIR FORCE INSTITUTE OF TECHNOLOGY

Wright-Patterson Air Force Base, Ohio

The views expressed in this thesis are those of the author and do not reflect the official policy or position of the United States Air Force, Department of Defense, or the United States Government.

AFIT/GAE/ENY/05-M03

Boundary Layer Flow Control Using Plasma Induced Velocity

THESIS

Presented to the Faculty

Department of Aeronautics and Astronautics

Graduate School of Engineering and Management

Air Force Institute of Technology

Air University

Air Education and Training Command

In Partial Fulfillment of the Requirements for the

Degree of Master of Science in Aeronautical Engineering

Brian E. Balcer, B.S.M.E.

2Lt, USAF

March 2005

AFIT/GAE/ENY/05-M03

Boundary Layer Flow Control Using Plasma Induced Velocity

Brian E. Balcer, B.S.M.E.
2Lt, USAF

Approved:

/signed/	10 Mar 2005
Dr. M. Franke, PhD (Chairman)	date
/signed/	10 Mar 2005
Lt Col E. J. Stephen (Member)	date
/signed/	10 Mar 2005
Maj R. J. McMullan (Member)	date

AFIT/GAE/ENY/05-M03

Abstract

An examination of the effects of plasma induced velocity on boundary layer flow was conducted. A pair of thin copper film electrodes spanned the test section, oriented at thirty degrees from normal to the free stream flow. An adverse pressure gradient was imposed over the electrode configuration using a pressure coefficient profile similar to that associated with suction side of a Pac-B low pressure turbine blade. In addition, suction was applied to keep flow attached on the upper wall, inducing separation over the electrode. The electrode is supplied by an AC source at three different power levels with the free stream flow at three separate chord Reynolds numbers. The chord length was based on the geometry of the simulated airfoil profile used for the upper wall of the test section. The flow turbulence intensity was varied by means of a passive grid in the upstream flow. Velocity data were collected using particle imaging velocimetry as well as with a boundary layer pitot probe. The power levels applied to the plasma were between 20 and 40 watts. The flow regimes studied were between chord Reynolds numbers of 50,000 to 100,000. It was found that the use of plasma to control the boundary layer enabled the flow to remain attached in the presence of an adverse pressure gradient. However, at the studied Reynolds numbers and electrode configuration the plasma was unable to affect an already separated flow regardless of the power input to the electrode. It was finally ascertained that two types of turbulent structures could be resolved, one being a counter-rotating vorticity pair and the other being a counter-rotating vorticity sheet.

Acknowledgements

I would like to thank the folks at AFRL/PRTT for letting me use their facilities and providing me with the tools to conduct the research. I owe a debt of gratitude toward two specific individuals without whom I wouldn't have had this great opportunity. First, I would like to thank Dr. Richard Rivir at AFRL/PR for the guidance and suggestions throughout. Second, I would like to thank my thesis advisor, Dr. Franke, who suggested this research topic based on several conversations we'd had when I initially arrived at AFIT.

Brian E. Balcer

Table of Contents

Page

List of Figures

List of Tables

List of Symbols

Symbol		Page
Re	Reynolds number	16
A	Constant for Reynolds number to Nusselt number correlation	17
B	Constant for Reynolds number to Nusselt number correlation	17
Re_d	Reynolds number based on hot film diameter	17
n	Constant used for Nusselt number approximation	17
A	Area	17
l	Length	17
k_{th}	Thermal conductivity	17
H_f	Heat lost to surrounding fluid	17
R_w	Resistance of wire in flow	17
R_f	Resistance of wire with no flow	17
T_w	Temperature of wire in flow	17
T_f	Temperature of wire with no flow	17
E_{hf}	Voltage across hot film anemometer	17
I_{hf}	Current through hot film	17
A'''	Constant for voltage to velocity correlation	18
B'''	Constant for voltage to velocity correlation	18
Δp	Differential pressure	33
u_e	Eddy velocity	35
t	Time	35
u	Horizontal velocity	40
v	Vertical velocity	40
Re_c	Reynolds number based on modelled chord length	42
Re_θ	Momentum thickness Reynolds number	53
θ	Momentum thickness	86
ρ	Density	86
μ	Viscosity coefficient, viscosity	86

List of Abbreviations

Boundary Layer Flow Control Using Plasma Induced Velocity

I. Introduction

The quest for increasing the efficiency of turbine engines has taken many paths. One of the many areas where an engine designer can increase efficiency is in the design of blading with increased loading. To this end there have been numerous methods proposed that control separation losses and circulation around blading. This research effort is an attempt to determine and improve the range of application of atmospheric glow discharges as viable flow control mechanisms.

1.1 Background

The use of a plasma to control boundary layers studied in low speed wind tunnels has been used for a number of years. In 1998, researchers at the University of Tennessee created a blue print for the types of electrodes that work best when dealing with plasmas at atmospheric pressure. Roth, et al. [17], patented the One Atmosphere Uniform Glow Discharge Plasma (OAUGDP). They demonstrated that electro-hydrodynamic (EHD) forces could be generated with sufficient magnitude to alter wall turbulence and drag. More recent studies by Volino and Hultgren [21], and Ashpis and Hultgren [8], show that while using plasma, significant effects could be seen when dealing with the separation on the aft portion of the suction side of a low pressure turbine (LPT) blade. Using a phased plasma actuator that consisted of five electrodes, Volino and Hultgren demonstrated that a plasma would in fact counter the effects of separation and keep the flow attached at Reynolds numbers (Re) greater than 50,000. They found that at Re $\approx$ 50k the pressure coefficient (C_p) profile would indicate a separated flow on the adverse pressure gradient portion of the test surface. Furthermore, with the plasma actuator on the flow would remain attached and the measured C_p profile was in excellent agreement with the theoretical profile at higher

Re. The majority of studies conducted in the past have been accomplished with the electrodes oriented perpendicular to the free stream. Usually an array of several electrodes parallel to each other were used. Another study, which was conducted at the Air Force Research Lab (AFRL), dealt with the effects of alternating current (AC) plasmas on an attached boundary layer. In it Jacob, et al. [9] showed that the plasma clearly accelerated the flow in both the vertical and axial directions near the wall as the flow passed in close proximity to the plasma. The electrode used in the current study was a single thin film copper electrode pair with one electrode on the top surface of a circuit card and the other electrode on the bottom of the circuit card with the trailing edge of the upper electrode being aligned with the leading edge of the lower electrode. The electrode spanned the test section with the major axis being oriented thirty degrees from normal to the free stream flow. The electrodes used by Jacob et al. [9] and Van Dyken, et al. [20] were an array of several electrodes configured as described above, aligned normal to the flow. This was also the setup Roth, et al. called asymmetric staggered [18]. The goal of electrode design is to maximize the force on the charged particles. The force, F_p, is proportional to both the dielectric constant, k, of the medium where the electrons are located (in this case air) as well as the gradient of the voltage, E^2, across the electrodes, i.e.

$$F \propto k\frac{\partial E^2}{\partial x}.$$

Van Dyken et al. [20] were studying the effects of the dielectric thickness, electrode type, input voltage, input frequency, as well as input waveform. They concluded that a thicker dielectric was best due to its ability to handle higher voltages prior to catastrophic failure and also that there was a peak operating frequency which gave a maximum performance in terms of net force production [20].

Studies have also been conducted in an attempt to model OAUGDP and make the plasmas operate at peak power. Chen [5] explained two different types of impedance matching networks, one applied to the secondary side of a transformer and one ap-

plied to the primary side of a transformer. Chen [5] noted that there were several advantages of the primary side matching circuit over the secondary side network. The benefits stem from the lower voltages present in the primary of the transformer. The lower voltages need less robust circuits and the resulting impedance from the necessary inductor coil would be less. Conversely, Chen [5] stated that if the capacitance of the plasma was of low enough magnitude, the inductance necessary would be too small causing large currents through the inductor and transformer primary.

The plasma structure itself analyzed by Enloe, et al. [6] was found to have a definite pattern to its formation and subsequent quenching. The authors found that during each half period of the input voltage, the plasma would evolve in a spatial and temporal dimension. In the temporal mode, the authors described a quenching and ignition phase. In the spatial mode, an expansion phase as well as another ignition phase were discussed. Further discussion of this will be covered in Section 2.2.

Roth et al. [18] demonstrated what appeared to be unsteady streamwise vortices. The authors emitted streak lines from a smoke wire apparatus immediately upstream of and approximately 5 mm above an array of parallel electrodes. The electrodes were oriented along the free stream flow axis so that the streak lines and electrodes were initially parallel. It was shown that titanium dioxide smoke streak lines initially converged to the electrodes then subsequently showed turbulent mixing. Roth et al. [18] attributed the attraction and mixing phenomena to paraelectric effects. The paraelectric effect theory was further strengthened by comparing the effects when the root mean squared (RMS) voltage was 3 kV to when it was 5 kV. The difference was that the mixing of the streak lines took place further upstream at 5 kV.

Turbulence generated at a wall typically results in sub-layer turbulence intensity (TI) levels of 8 - 12%. Free steam turbulence alters these near wall TI levels as well as the heat transfer effects near the wall. Because of these alterations, it is of interest to examine TI effects on the properties of the discharge and its subsequent effects on the near wall electrical flow interactions. In the current study, it was desired to have

different levels of turbulence intensity. In addition, Volino and Hultgren [21] explain that different turbulence levels are encountered by the LPT blades during different phases of flight. Turbulence can be produced by several of methods, usually based on the type of apparatus used to create the turbulence. The formulations of Roach [16] are commonly used models which treat several grid types and geometries. Roach produced empirical equations for each type of turbulence generating geometry that was used. He studied both the pressure drop across the devices used to generate the turbulence as well as the decay characteristics of the turbulent structures. Roach's empirical results were used to design and predict the levels of turbulence employed in this experiment.

1.2 Objective

This research effort is aimed at determining the benefits of using an electrode oriented thirty degrees from normal to the flow. The electric field produced by the atmospheric glow discharge plasma will induce a velocity component normal to the electrode. The normal velocity component will tend to create a vortex whose axis of rotation is parallel to the electrode. The primary flow will impose a velocity in the flow direction. The resultant of the vortex created by the electrode and the interaction between it and the free stream flow, will be a vortex that sheds off from the electrode initially oriented in the same manner as the electrode with respect to the free stream flow. As the vortex convects downstream, the free stream flow will eventually tend to break the vortex up. The objective of this research was to determine if a vortex oriented with a component in the free stream direction could be sustained as it was convected downstream. Also, if such a vortex was present, was it a better boundary layer control mechanism than a vortex created by an electrode oriented normal to the flow. The effects of the offset electrode on the boundary layer were to be studied in the presence of an adverse pressure gradient consistent with the suction side of a "Pac-B" LPT blade. In completing the aforementioned objective, a measurement and automation apparatus was created that could be utilized for subsequent research

projects. Both the setup and verification of the measurement hardware and software had to be completed in order to begin the data collection process.

1.3 Organization

The research effort will be presented by first explaining the theory behind several of the different phenomena that need to be understood in order to successfully conduct the experiment. The following sections deal with the experimental setup, including all facilities, hardware, software, and measurement devices utilized throughout the research. The procedure used to create the electrode is outlined. The plasma created and used in this study will be characterized by the values of voltage and current applied. Impacts of a given voltage and current on other plasma characteristics are discussed. Setup and operation of the particle imaging velocimetry (PIV) equipment used is explained. The test matrix used to quantify the objectives will be explained. Results of the data collection process are examined and conclusions are drawn as to the effectiveness of the electrode configuration used in this study. Finally, recommendations for future research are discussed.

II. Theory

The safe and efficient conduction of the experiment was predicated on having a working knowledge of all the processes that were involved. In order to gain the insight necessary, several areas of research had to be studied. A brief explanation of the aspects of each area pertaining to the research effort are given below. The explanations given here are by no means all inclusive, the references cited could lend better insight to those wishing to obtain a more in-depth knowledge of the topics discussed.

2.1 Boundary Layers

In 1904 L. Prandtl coined the term boundary layer or frictional layer [19]. When bodies are immersed in a fluid flow, pressure and friction forces act on the fluid in the vicinity of the body. For a simple flat plate shape, a laminar boundary layer will begin to develop at the leading edge. As the flow traverses downstream, the boundary layer will undergo a transition to laminar-turbulent flow. Even further downstream the flow will become fully turbulent. Each of these regimes has its own unique characteristics which define how the boundary layer will grow. These changes in the flow can be attributed to the effects of internal forces in the boundary layer as well as external forces outside of the boundary layer. The internal forces are mainly attributed to viscosity and friction. In laminar flows, the boundary layer grows due to the viscosity of the fluid. Turbulent flows however have a turbulent or often called frictional layer as well as a thin viscous layer immediately above the wall [19]. For an airfoil, additional pressure forces also affect the growth of the boundary layer. The free stream flow around the airfoil imposes a pressure gradient at the edge of the boundary layer. The pressure at each axial location along the airfoil is the same as the pressure at the edge of the boundary layer perpendicular to that point [19]. A consequence of this is that the pressure gradient imposed by the outer flow would have a marked effect on boundary layer growth.

Turbine engines have many sets of blades. There are fan blades, low pressure turbine and compressor blades, and high pressure turbine and compressor blades. In a compressor or turbine section there are alternating sets of rotors and stators. The rotor blades are rotating on a disk which is comprised of many blades. The stators are stationary and act to direct the air flow into the following rotor section at the most efficient angle [24]. Each of the blades on the rotor disks resemble an airfoil. An example of a high pressure turbine (HPT) blade is shown in Figure 2.1. Each

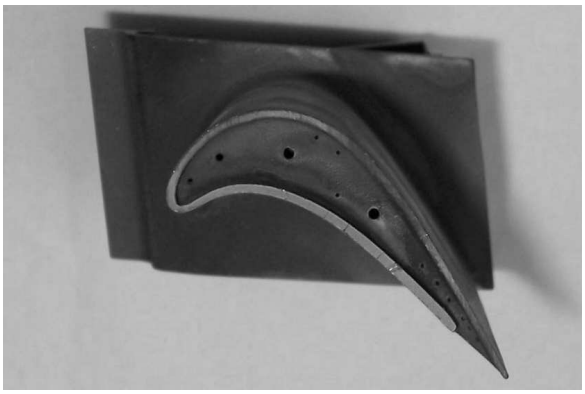

Figure 2.1: Typical HPT blade.

airfoil has a suction and a pressure surface. The bottom side of the blade shown in Figure 2.1, is called the pressure side. There is a favorable pressure gradient there and the flow will tend to remain attached. Conversely, the upper surface is a suction surface and the flow will tend to separate. Schlichting [19] describes the flows tendency to separate by relating energy. In the case of the turbine blade, as the flow impinges on the leading edge of the blade, the flow is accelerated to get up and around the top of the blade. The pressure energy is converted into kinetic energy as the flow accelerates. The frictional boundary layer acts on the flow over it by absorbing some of the kinetic energy, converting it into heat or other sources. Once the flow reaches the top of the airfoil, the kinetic energy starts to be transferred back into pressure energy. As the flow decelerates on the aft section of the blade, the remaining kinetic energy is transferred back into pressure energy. As a result of the losses to the boundary layer, there is not enough energy to enable the flow particles to completely reach the trailing edge of the airfoil. The flow then stops and may

consequently start moving back on the airfoil, resulting in separation. To maximize the work out of or produced by a rotor, one would like to turn the air flow through a large angle. As the turning angle is increased, flow separation and adverse pressure gradients as described above are encountered. Plasma actuators are investigated to reattach these flows in an attempt to achieve the maximum work per rotor stage.

2.2 Plasma Discharge

The plasma generated for use in this research was very similar to that described by Roth [17] as a one atmosphere uniform glow discharge plasma. It was also explained by Enloe et al. [6] that the plasma was a surface configuration dielectric barrier discharge (DBD). The plasma was created by placing two slender long electrodes on each side of a thin dielectric plate. An essential aspect for the creation of the most efficient plasma is the configuration of the electrodes. In most references the configuration which yielded the most efficient results [6, 17, 18] was an asymmetric staggered configuration where the electrode on the bottom of the dielectric plate was immediately aft of the electrode on the upper part of the plate. The trailing edge of the upper electrode was coplanar with the leading edge of the lower electrode. A plot of $\frac{\partial E^2}{\partial x}$, where E^2 is the voltage, and x is the axial direction, would show that the asymmetric staggered arrangement produces the highest voltage gradients and resulting power. The electrode was supplied an AC signal operating at a given frequency, usually on the order of a few kilohertz with a voltage amplitude on the order of a few kilovolts as supplied through a transformer. Using Equations (2.1) and (2.2), the instantaneous resistance and capacitance of the plasma could be determined at each time step. For the resistance of the plasma, R_p:

$$R_p = \frac{V_m}{I_m}(1 + tan(\phi))^{-\frac{1}{2}}, \tag{2.1}$$

where V_m is the input voltage to the plasma electrode from the transformer secondary, I_m is the current measured via a current coil, and ϕ is the phase shift angle in radians

of the current lagging the voltage in radians. For the capacitance of the plasma, C_p:

$$C_p = \frac{1}{R_p \omega tan(\phi)}, \tag{2.2}$$

where ω is the input frequency as set on the HVPS.

As a result of a breakdown, or electron avalanche from one electrode to the other, the current has an erratic behavior that can include large changes in value for extremely small time steps. The mean of the signal retained a sinusoidal waveform, but the magnitude could be very erratic if sampling at a short enough time step. As a result of this, in order to obtain smoother plots a 100 point moving average was used to smooth the data. An example of the raw (lighter) and smoothed (darker) data is shown in Figure 2.2. The smoothed data was used in Equations (2.1) and (2.2) to

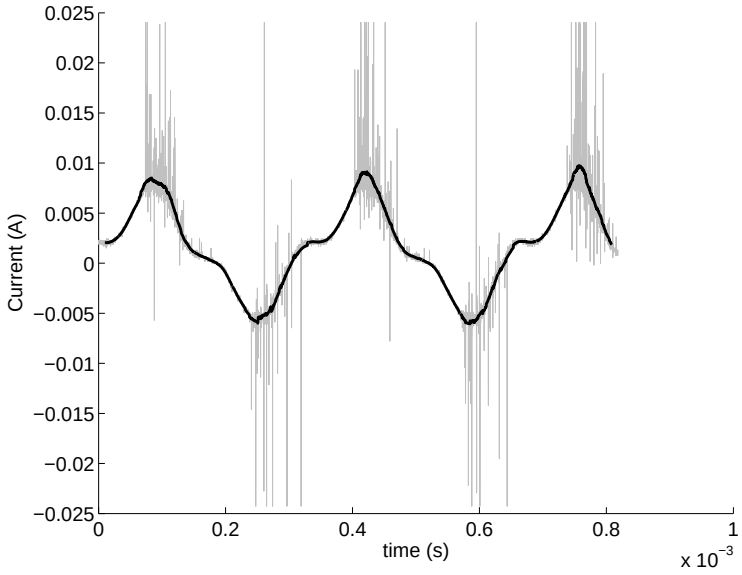

Figure 2.2: Current trace comparing rough and smoothed values.

calculate C_p and R_p. The power computed using the aforementioned equations should closely resemble the power P measured via Equation (2.3).

$$P = IV. \tag{2.3}$$

Where I and V were taken directly from the instruments in the experiment. An equation for P which used the value of R_p derived from Equation (2.1) was

$$P = I^2 R_p. \tag{2.4}$$

The results from Equations (2.3) and (2.4) are included in Appendix C.

It was discovered by Enloe et al. [6] that a plasma went through distinguishable phases of growth and decay in both a temporal and a spatial mode during each half period of the supplied waveform. As mentioned in the previous section the phases in the temporal mode were ignition and quenching, and in the spatial mode were ignition and expansion. For use in visualizing the phases, the reader is referred to Figures 4 and 9 of Enloe et al. [6]. To recapitulate, in the temporal mode, at the extremum of the voltage trace the plasma quenches, a result Enloe et al. [6] say is due to a lack of ions to recombine. As the voltage signal progresses in time, the voltage begins increasing in magnitude. As long as this increase keeps changing in a positive direction, the plasma can remain. As the magnitude reaches a local maxima, the plasma no longer has ions available and the plasma quenches. Figure 2.3 shows where the theoretical plasma phases occurred on voltage data taken during the current study. Also studied by Enloe et al. [6], was the spatial structure of the plasma using photoelectric observations. They found that the plasma is densest at the ignition phase and trails off during the remainder of the voltage sweep. The authors called this the "expansion phase" of the plasma discharge. Further, the spatial structures were non-uniform with denser regions nearest the electrode. Also, the plasma itself ignited farther downstream of the electrode nearest the outer edges of the electrode. Again, refer to Figure 9 in Enloe et al. [6].

As mentioned in the Section I, large gains could be realized if the impedance of the plasma were matched to the output of the power supply. According to Chen [5] the goal of matching the impedance of the plasma was to maximize the power delivered to the plasma from the source. To this end, he determined that the plasma impedance

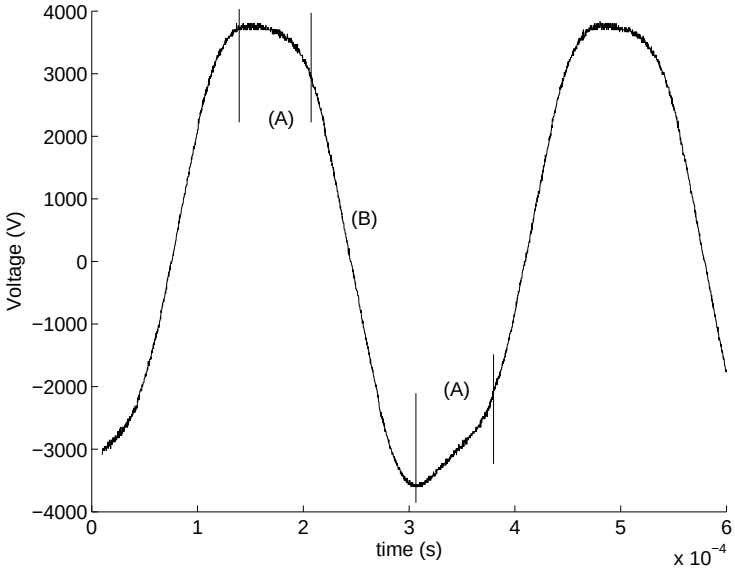

Figure 2.3: Voltage trace showing (A) quenching and (B) ignition phases.

needed to be seen as purely resistive by the output terminals of the transformer or power supply. The end goal of impedance matching is to attempt to minimize the circulating current through the power supply. Minimizing the circulating current will result in the plasma acting as pure resistance. The task of matching the impedance is to determine what combination of devices is necessary to adjust the impedance to a proper value. The noticeable result of using the impedance matching network was that the discharge current was increased, thus maximizing the power output. Chen [5] showed that by matching the impedance of his network on the secondary side of the transformer, he was able to raise the plasma current by almost an order of magnitude. In order to make the plasma or transformer appear as a purely resistive load, one has to make the imaginary (time dependent) part of Equation (2.5) go away.

$$V = IR + jI\left(\omega L - \frac{1}{\omega C}\right) \tag{2.5}$$

Equation (2.5), found in Kraus [12] determines the voltage (V) given the current (I), the frequency of the input voltage (ω), the inductance (L), and the capacitance (C). As can be seen, if the term in the parenthesis is exactly zero, the imaginary part

is eliminated and the load is purely resistive. For the electrode configuration used, a theoretical method of determining the approximate capacitance of the plasma was desired. A method that was attempted as an approximation for the capacitance (C_{pl}), was one using flat plate capacitor theory. This theory is based on the equation,

$$C_{pl} = k\epsilon_0 \frac{A_{pl}}{d_{pl}} \tag{2.6}$$

where k is the dielectric constant of the material, ϵ_0 is the permittivity of free space, A_{pl} is the area of the plates which overlapped, and d_{pl} is the displacement between the two plates. The underlying assumption of the flat plate capacitor equation is that the majority of the field strength lines between the plates will be normal to the plates and parallel to each other, see Figure 2.4. The field strength lines which loop around from

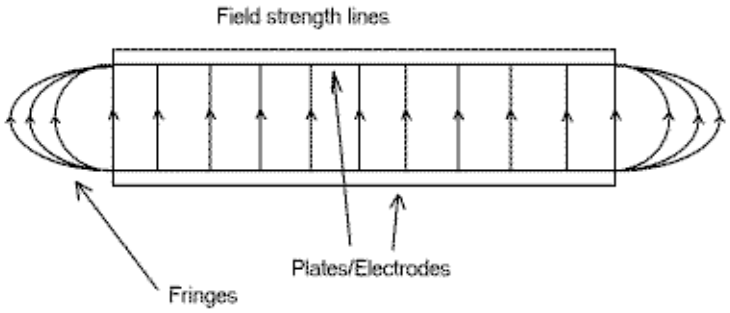

Figure 2.4: Schematic of field strength lines between two parallel flat plates.

the outer edge of one plate to the other in an arc are called the fringes. The basis of the theory is that these fringe effects can be negated without serious repercussions on the determined capacitance. As an asymmetric configuration [17] is arranged, the field strength lines between the electrodes will be dominated by fringe effects. Thus, it was determined that the aforementioned theory would not yield the proper capacitance.

To determine the theoretical capacitance, a more in depth analysis would need to be undertaken.

2.3 Turbulence Generation and Decay

HPT blades generated TI levels of 10 - 20%. LPT blades generate TI levels of 4 - 6%. LPT separation control is of primary interest so TI levels of 4 - 8% were chosen for this study. The goal in creating turbulence in a low speed wind tunnel is not only increasing the TI to a certain level, but to create an isotropic TI. That is, turbulence that is very nearly the same over the individual cross section of the wind tunnel perpendicular to the free stream. As mentioned before, Roach [16] tested several configurations of turbulence generating grids as well as blown jet grids. Roach's equations for TI were derived using empirical data each having a length term raised to the negative five sevenths. Roach derived the following equation for TI

$$TI = C_{turb}\left(\frac{x}{d}\right)^{-5/7} \tag{2.7}$$

where C_{turb} is a constant derived from the geometry used to create the turbulence (not to be confused with capacitance), x is the distance downstream from the grid, and d is the representative grid dimension. Roach found that for a square mesh of square bars such as that used in the present experiment, the constant C_{turb} above should be 1.13 [16]. Roach further theorized that the TI would be independent of Re as long as it remains between $10^2 < Re < 10^4$. The Re limitation was from the range of Re that Roach studied, not necessarily true limits on the phenomena observed. The TI computed using Equation (2.7), will decay in the direction of increasing distance from the turbulence generating mesh due to the negative exponent and should remain nearly isotropic. The value actually used for C_{turb} in the present experiment was based on the results obtained by Bons et al. [2], who used the same tunnel for another study. The value derived was $C_{turb} = 1.46$. In Schlichting [19], turbulence intensity is defined

as

$$TI = \frac{\sqrt{u_{fl}^2}}{U}, \tag{2.8}$$

where u_{fl} is the fluctuating velocity component in the streamwise direction and U is the free stream velocity. The use of Equation (2.8) can be extended to three dimensions.

2.4 Particle Imaging Velocimetry

Particle Imaging Velocimetry (PIV) is based on taking two pictures of a test area with a known time interval between the images. The flow area is visualized by inserting seed particles upstream of the test area which are convected with the flow. The seed particles were created by boiling propylene glycol off of one of three heating elements. In order to conduct a PIV based experiment, three main pieces of equipment have to be utilized. First, a laser must be positioned such that the beam is optically altered from a beam to a thin planar laser sheet focused at the point where the images are to be taken. The laser must be of sufficient power to illuminate the particles. The laser must also be able to fire rapidly in order to produce two distinct pulses of light which are synchronized with the aperture of a photo capture device. There are both two dimensional and three dimensional PIV setups, the latter usually requiring two separate laser heads mounted at different locations. The next critical piece of equipment was a high speed digital camera. The camera must be setup so that the image is in focus exactly where the laser sheet crosses its field of view. To complete the PIV process, a flow visualization software was used. The flow visualization software uses the images captured via the high speed camera. The images are imported to the flow visualization software, velocity vector maps are then created using successive images taken at a known time interval apart. The images can be recorded in one of two modes, the first being double frame mode. Double frame mode takes a series of image pairs with a known time interval between them. The correlation software only relates the two images of the pair. The correlation software

does not relate one image pair to another image pair, so the timing between pairs is not important. This allows the laser to recover longer than if fired rapidly at the frequency necessary to obtain the optimal time between images. The second mode is where the camera and laser constantly fire at the same frequency, perhaps with a small delay between the camera aperture opening and the laser firing. The small delay will alow the aperture to be open when the particles are illuminated by the laser. In this mode all images are recorded. Depending on image size, vast amounts of memory can be filled in a very short period of time. The resulting images will then be imported into another program to complete the PIV process.

The flow visualization software used in conjunction with PIV will take the images and use correlation algorithms that determine the distance each particle has travelled between each image. The maximum expected velocity of the flow field must be known with relative certainty. Also, the use of PIV is usually limited to small wind tunnels at low speeds [1]. One of the more important pieces of information which needs to be determined for proper PIV results is the dynamic range. The dynamic range is determined by dividing the pixel resolution by the pixel displacement for each time step. That is, if one were to resolve down to a 0.5 pixel resolution with the particle travelling 15 pixels between images, the dynamic range would be 30. If the dynamic range was not of sufficient magnitude, the time between light pulses would have to be decreased. As a result of firing a laser at high frequency, its output power is decreased. The dynamic range can be increased by using adaptive correlations. Adaptive correlations are correlation routines that are used in examining the PIV data in order to extract velocity data. The adaptive correlation is an improvement upon the cross correlation routines by using an iterative process that enables the result of more valid vectors with an increased image size and dynamic range. The pitfalls of using adaptive correlations can be a larger impact from noise as well as less accurate velocity measurement due to less vectors on which to base an average.

2.5 Hot Film Anemometry

Hot film anemometry has been used for many years. The basic concept behind hot film anemometry is much the same as hot wire anemometry. The difference between the two is that the hot film version is made by depositing a thin layer of metal onto an insulating ceramic substrate [22]. The size of the hot film sensor is larger than that of a hot wire and is less prone to destruction via small particles in the flow field. Hot film anemometry can be undertaken in one of two methods, the first being constant temperature and the second being constant current. Constant current was not used and as such will not be discussed. In constant temperature anemometry a feedback amplifier is used to sense the unbalance in a Wheatstone bridge and in turn adjust the driving voltage in order to keep the bridge balanced. The constant temperature arrangement can be used to measure phenomena with frequencies of up to 400 kHz [22]. The equipment used in the present study was only capable of measuring frequencies up to 20 kHz. Constant temperature anemometry (CTA) is predicated on the fact that using the Wheatstone bridge, the resistance of the sensing element is directly proportional to the temperature of the film. When the film is immersed in a fluid, its temperature is altered due to the heat transfer between the element and its surrounding medium. The heat transfer causes a change in the resistance of the element and as stated before the amplifier will then adjust the driving voltage to balance both legs. In order to derive a velocity from a voltage measurement, a correlation has to be used. An equation relating the heat transferred from the element as a function of fluid type and flow velocity is used. The equation was derived by King [11] and is shown below as presented by Kays and Crawford [10]:

$$Nu = 0.42Pr^{0.2} + 0.57Pr^{0.33}Re^{0.5},$$

where Nu is the Nusselt number, Pr is the Prandtl number, and Re is the flow Reynolds number. Since for a given fluid at a given temperature Pr is constant, the

previous equation can be re-written as [3],

$$Nu = A + BRe_d^n,$$

where A and B are constants to be determined, Re_d is the Reynolds number based on hot film diameter, and n is approximated as 0.5. Also in Kays and Crawford [10], the Nu is defined as

$$Nu = \frac{lH_f}{Ak(T_w - T_f)}$$

which with area (A) and length (l) being constant with a fluid thermal conductivity, k_{th}, can be reduced to

$$const \cdot Nu = \frac{H_f}{T_w - T_f},$$

where H_f is equal to the heat lost to the surrounding fluid media, which is proportional to the power input to the wire, namely I^2R_w. The resistance of the wire in the flow and resistance of the wire with no flow, R_w and R_f respectively, are both functions of temperature, namely T_w and T_f. With these previous two results, it can be seen that

$$\frac{H_f}{T_w - T_f} \propto \frac{I^2R_w}{R_w - R_f}.$$

Also, recall

$$E_{hf} = I_{hf}R_w$$

where E_{hf} is the voltage from the anemometer, I_{hf} is the current through the film, so

$$E_{hf}^2 = I_{hf}^2R_w^2.$$

With these facts and the assumption of constant current, King's law can be restated as shown below,

$$\begin{aligned} Nu &= A + BRe^n \\ \frac{lH_f}{Ak(T_w - T_f)} &= A + BRe_d^n \\ \frac{H_f}{(T_w - T_f)} &= A' + B'Re_d^n \\ \frac{I^2 R_w}{R_w - R_f} &= A' + B'Re_d^n \\ \frac{I^2 R_w^2}{R_w - R_f} &= R_w(A'' + B''Re_d^n) \\ \frac{E^2}{R_w - R_f} &= R_w(A'' + B''Re_d^n) \\ E^2 &= R_w(R_w - R_f)\,(A'' + B''Re_d^n) \end{aligned}$$

which for a given velocity and temperature can be re-written as,

$$E^2 = A''' + B'''U^n, \tag{2.9}$$

where E is the voltage displayed on the anemometer, U is the velocity of the fluid, and n is an exponent whose value typically lies between $0.4 - 0.6$ [3] and relies on Re_d as defined above. A''' and B''' are constants to be found through calibration.

2.6 Photofabrication

In order to study the effects of plasma discharges, electrodes had to be fabricated. This section explains the steps taken to create the electrode used in the present study. Photofabrication is a generally-used term to represent a set of steps undertaken to create printed circuit cards. The process of photofabrication contains several underlying processes, the first of which was getting an electrode material on the surface of a circuit board. Circuit boards are typically made of epoxy-glass, fabric, epoxy-paper, phenolic-paper, polyimide-glass fabric, PTFE-glass fabric, and other moldable

plastics [7]. The manufacturer of the circuit boards will usually bond copper foil to the surface of the substrate via direct bonding and provide different thicknesses of electrode material to the consumer depending on need. The thickness is determined by the mass of copper deposited per square foot, typically 0.5 oz/ft^2 to 2 oz/ft^2. The copper is protected by a material called photoresist. The photoresist acts as a barrier between the copper to be used as an electrode and the materials used to remove the unwanted copper. The photoresist is bonded to the copper by exposing it to high energy ultra violet (UV) light. The bonded photoresist is harder than the unexposed variety and as such will not come off as easily with a developer solution. It should be noted that there are two types of photoresists. The first is a positive working and the second is a negative working photoresist. The former is used when the exposed photoresist is rendered soluble to the developers in the exposed region [7], whereas the latter is used when the photoresist renders the exposed area more resistant to the developing solution. The unwanted electrode material is removed via a chemical reaction with an etchant and the final product is a bare circuit board with a copper film electrode visible.

III. Experimental Setup and Procedure

There were several pieces of equipment that needed to work in concert for the experiment to be a success. The most important topics are described below. Following the description of the facilities, the procedure utilized for data collection is explained.

3.1 Wind Tunnel

3.1.1 Tunnel Setup. The wind tunnel used was a modified version of the tunnel used by Jacob et al. [9] and Rivir et al. [15] in two previous studies. Figure 3.1 is a schematic of the tunnel and Figure 3.2 is a photograph of the tunnel looking down from the exhaust end. The tunnel was essentially an open circuit low speed wind

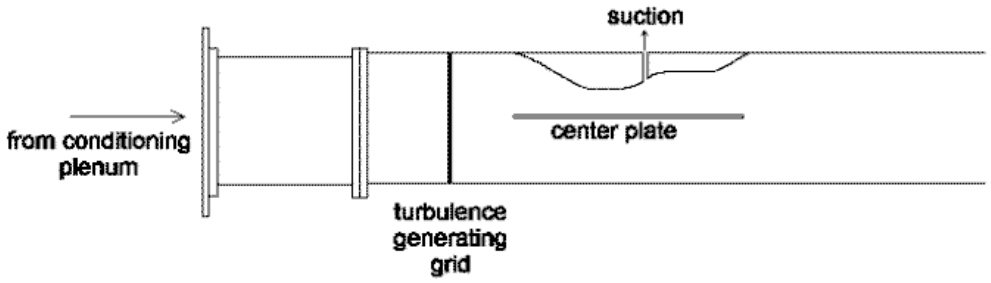

Figure 3.1: Schematic of tunnel used for experiment.

tunnel. The blower section was situated prior to the test section. The tunnel could operate on one of two compressors and was parallel with two other flow paths, each of which could be utilized alone or altogether depending on the position of two air controlled valves. Temperature control was attained using a chiller section. All of the present research was conducted at 60^{o}F. The operating air velocity of the section used in this research was from 3 m/s to approximately 10 m/s, but it was noted by Rivir et al. [15] that the velocity could reach as high as 80 m/s with an isotropic turbulence intensity within one percent across the test section. The tunnel cross section could be altered slightly in the vertical axis, but for the research documented here was 36

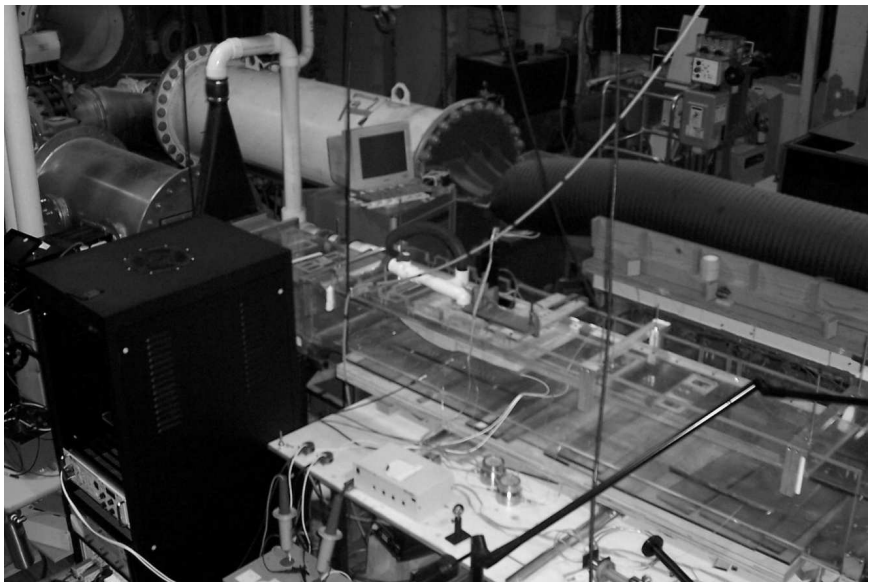

Figure 3.2: Photograph of tunnel used for experiment.

cm wide and 23 *cm* tall. The inlet to the tunnel was a larger cylindrical reservoir with flow straighteners as well as an opening for injection of seed particles prior to entering a round to rectangular divergent duct which routed the flow into the test section. Also available for turbulence generation and suction were two separate blower motors as well as a ShopVac vacuum. One blower motor provided air to a jet cross flow turbulence rig. The cross jets were not used for turbulence generation due to the blown air altering the tunnel velocity and not allowing the seed particles past for PIV use.

3.2 Test Section Apparatus

3.2.1 Mid Tunnel Test Section. The tunnel was configured with a was 1.27 *cm* thick by 69.85 *cm* long plexiglass plate that spanned the test section and was suspended midway between the upper and lower tunnel walls, see Figure 3.3. The plate had a 4:1 elliptical leading edge and a movable flap on the aft section that could be used to alter the velocity on the top surface without having to throttle the valve at the inlet to the tunnel. There was a 1.8 *mm* deep recessed portion in the center of the

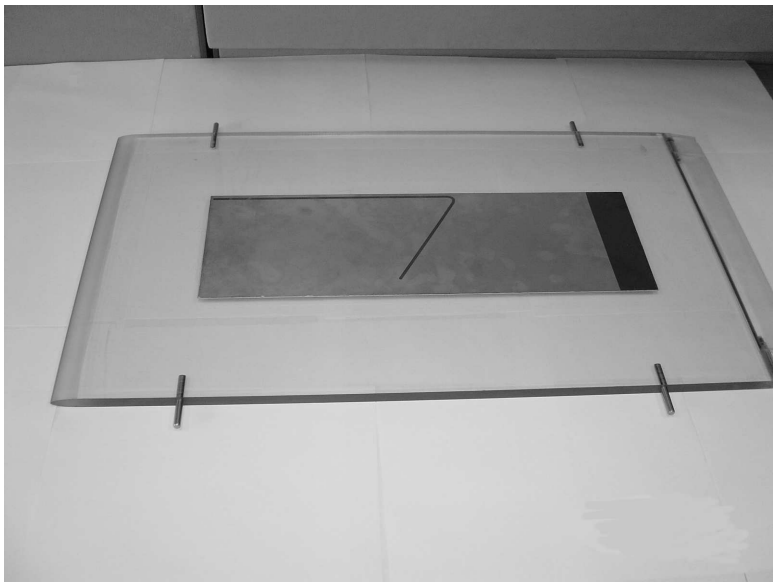

Figure 3.3: Center plate used to support the electrode.

plate to receive the electrode. This configuration was adapted from a representation of work done by Hultgren and Ashpis [8] as well as Volino and Hultgren [21].

3.2.2 Upper Wall Model. A method of imposing a modeled C_p profile of a Pac-B LPT blade over a flat test surface was needed. To do this, the upper wall was shaped from a block of polystyrene using a hot wire cutter in such a way so as to create a contraction and expansion region that would in turn alter the dynamic pressure over the flat plate. The resulting shape is shown in Figure 3.4. The C_p data was supplied and using it and flat plate boundary layer theory, the area at certain chord positions was determined to model a proper pressure differential between total pressure above the plate and the static pressure as measured on the sidewall of the tunnel. Also shown in Figure 3.4 are three black marks on the bottom of the upper wall model. The marks are reference points of 0, 65, and 100% chord, respectively. When the wall model was initially installed, it was unsure whether or not suction would be necessary to maintain attached flow on the downstream side of the contraction. In order to test for separation, pieces of mylar tape (cassette tape) were used as tuft material, see Figure 3.5. The mylar tape proved to be a superb material to use as a flow visualization device, even the slightest flow would make the strips lie down on

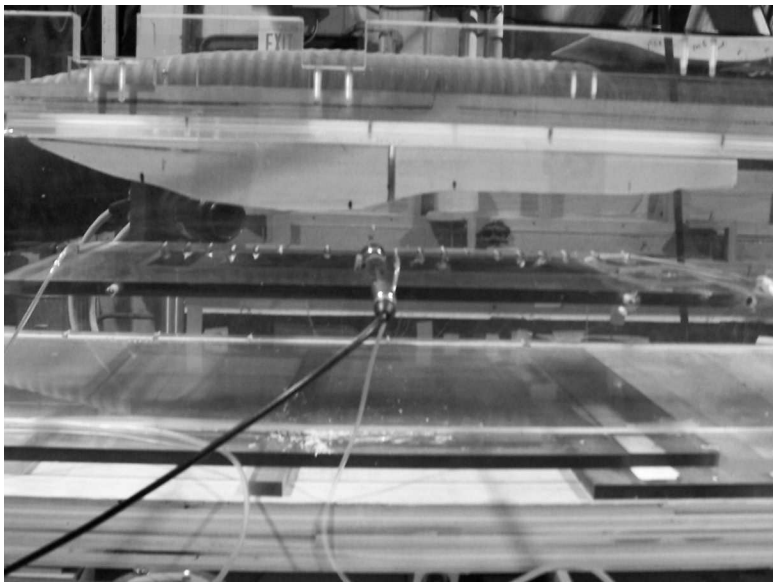

Figure 3.4: Geometry used to create separation.

the surface. Conversely, any reversal or stagnated flow would allow them to raise. It was found that the flow would not stay attached on the upper surface without upper wall suction. The suction on the upper surface was supplied by a 2 HP Shop Vac vacuum. The vacuum hose was inserted into one of two possible locations on the suction duct shown in Figure 3.6. The apparatus was made with 2 *in* PVC piping and fittings along with a 2 *in* manual ball valve. The pipes were epoxied to a wooden mount that directed the air from the slit in the polystyrene to the suction ductwork. Depending on whether the vacuum was attached between the valve and the flow or with the valve between it and the flow, the amount of suction could be throttled from virtually no flow to the maximum allowed by the vacuum. At the Re_c numbers studied, the maximum amount of suction was necessary to create a sizable separation layer with which the plasma effects could be studied. Further modifications to the upper wall model were to cut two half inch wide slits long enough to shine the laser sheet onto the electrode. The laser head was positioned over the test section and the light shown down vertically atop the electrode. The slits were covered on the lower flow side using clear packaging tape to maintain the profile while still allowing the laser light to shine through.

Figure 3.5: Use of mylar strips as tufts.

3.2.3 Micro-Traverse. The boundary layer total probe was positioned using the 4 *in* and 8 *in* micro-traverse shown in Figure 3.7. The traverses were linked via a National Aperture, Inc. controller to a computer and controlled using LabVIEW. Each traverse had a sensitivity of 27,816 counts per centimeter and was used to take boundary-layer probe measurements at 0.2 *mm* increments. The probe itself was wrapped in electrical tape prior to mounting in the traverse in an effort to isolate it electrically due to its close proximity to the plasma. The traverse had two axes with which one could maneuver the probe, it could be moved both fore and aft in the tunnel as well as vertically. The lateral location had to be configured by hand and was secured via an in house manufactured plexiglass support.

3.3 Photofabrication

The circuit board was purchased as a large piece and cut down to the 45 *cm* x 15 *cm* size used for the experiment. The board was 62 *mil* thick double-sided copper clad fiberglass laminate with a 1 oz/ft^2 coating thickness (approximately 0.036 *mm*). The board was made from continuous woven-glass cloth impregnated with epoxy resin. The board complied with Mil-S-133949H-GFK. In the AFRL/PRTT Heat

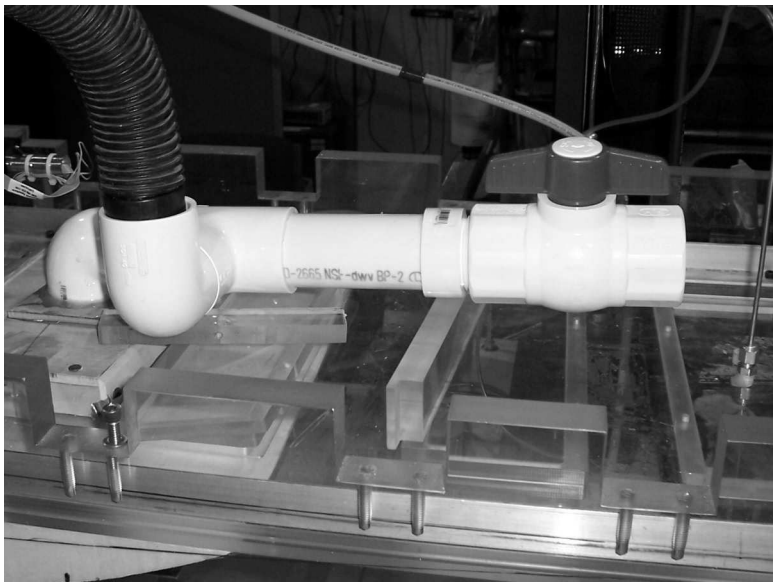

Figure 3.6: Suction apparatus used to keep flow attached on upper wall.

Flux Instrumentation Laboratory (Class 10,000 Clean Room with UV-filtered yellow lighting), a Dupont Riston FX 900 Series photoresist 30 micron thick was applied to both sides of the circuit board using the dry film laminator in Figure 3.8. Both sides of the circuit board had photoresist bonded to the copper and the photoresist was covered by a polyester film carrier that protected the copper from contamination or oxidation.

To create a pattern for the electrode, a simple negative was made on acetate paper. It was created so the non darkened part was in the shape of the desired electrode. The blackened part protected the rest of the photoresist so that it wouldn't be exposed to the UV light. The next step was to expose the photoresist so that it would protect the copper electrode material during subsequent etching processes. The electrode pattern, also called a phototool, was placed on the circuit board and then both the phototool and electrode were vacuum sealed on an exposure plate that ensured good contact between the two. The vacuum sealing also aided in ensuring no spurious light would partially expose other parts of the board. Figure 3.9 shows the device that housed the UV light. The top could rotate 180 degrees in order to

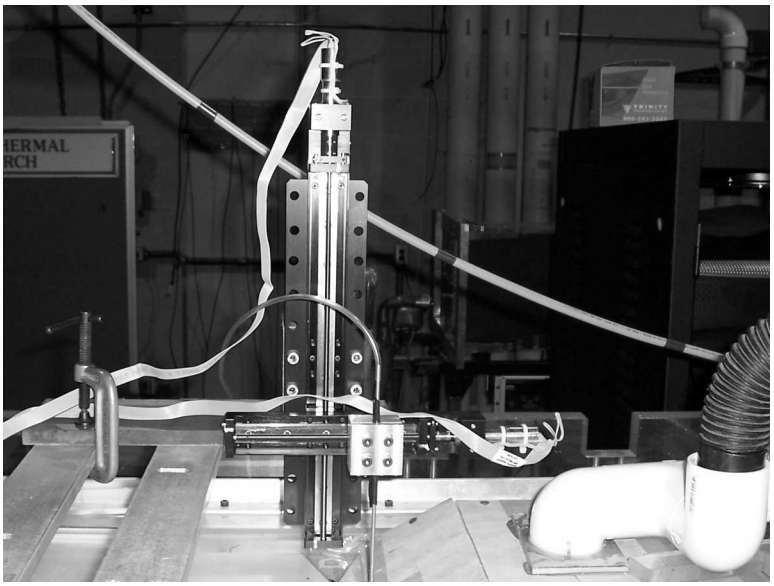

Figure 3.7: Microtraverse used to position boundary layer probe.

place the phototool directly over the UV light and also to protect the user from accidental exposure. After exposing the photoresist, a developing process was completed. The developing process was carried out to remove the unexposed photoresist from the copper. As described in Section 2.6, a negative acting photoresist was used. A developer solution of 0.9% sodium carbonate (Na_2CO_3) was used to rinse the unexposed photoresist off the circuit board, leaving the bare copper. The final process to remove the copper from the substrate is called etching. The etchant used was sodium persulfate ($Na_2S_2O_8$). The concentration of etchant to water was approximately one pound per gallon. The etchant was bath heated with an immersion heater and manually agitated in a rubber basin. The developing and etching processes were performed under the vent hood shown in Figure 3.10. This precaution was due to the possible vapors which could have been emitted from the solutions. It took several minutes to remove all the copper, most of which came off by simply agitating the water. A brush was used sparingly to aide in the copper removal. After all the copper was etched off, the electrode was rinsed and let stand to air dry at room temperature. After the removal of the photoresist at the ends of the electrode, the wires were connected to

Figure 3.8: Photoresist Dry Film Laminator.

the end with solder. Figure 3.11 shows the result of the photofabrication process, the electrode used to generate the plasma. A permanent black marker was used to darken the area where the laser would shine on the electrode. The black ink would absorb most of the light from the laser and help reduce reflection in the PIV images. The length of the plasma emitting portion of the electrodes were 141.3 mm long and 4 mm wide, resulting in an electrode area of 565 mm^2 with a vertical displacement of approximately 1.59 mm, the thickness of the circuit card.

3.4 Plasma Generation

An AC voltage was supplied to a transformer via a Titan high voltage power supply (HVPS). The frequency output was set to 3 kHz and the output voltage was varied between 100 - 130 V. The voltage signal was wired to the primary side of a transformer. The transformer was built by Industrial Test Equipment Company and could handle 0 - 250 $VRMS$ in the primary at 1 - 7 kHz and output -6 kV - 0 - 6 kV RMS to the secondary. A simple schematic of the electrical circuit is shown in Figure 3.12. The actual transformer modeled by Figure 3.12 is shown in Figure 3.13. The left side of the circuit from the transformer is called the primary, and the right

Figure 3.9: UV Exposure Unit with 3000W Metal Halide Bulb.

side is called the secondary. The capacitor and resistor on the secondary side labeled C_p and R_p represent the capacitance and resistance of the plasma, respectively. The AC voltage from each leg of the secondary was measured using Tektronix P6015A high voltage probes, each referenced to earth ground. The probes are labeled V1 and V2 in Figure 3.12, respectively. The current was measured via one of two Pearson model 4100 current coils. Each current coil outputted 1 V per amp measured and are labeled I1(t) and I2(t) in Figure 3.12 to remind the reader that these were measured as a function of time. The maximum peak current of the current coils was 500 A with a useable rise time of 10 ns. This latter limitation precluded the examination of the oscillatory behavior of the current when the breakdown occurs at plasma generation. The phase shift from the plasma had to be determined in order to calculate the power dissipated. To do this, two plots were compared, the first being the voltage and current trace with the load being a pure resistor, see Figure 3.14. The second plot was that of the voltage and current being applied to the plasma generating electrode, see Figure 3.15. It can be seen that the current lagged the voltage by approximately $3\pi/4$ radians so that value was used in Equation (2.1) as ϕ to determine R_p as well as C_p as displayed in Figure 3.12. Using a dosemeter, the plasma radiation was

Figure 3.10: Vent hood used while etching copper.

measured to be 27 $\frac{\mu rem}{hr}$ at a distance of approximately 20 cm directly above the electrode. This value was taken while the background was measured at 7 $\frac{\mu rem}{hr}$. In comparison, the average chest X-ray was found to be approximately 60 $mrem$ per procedure [14] and a CAT scan was quoted as 110 $mrem$ per procedure. So the radiation from the plasma was extremely low.

3.5 Particle Imaging Velocimetry

3.5.1 Laser and Light Arm. The laser used for PIV was a Pegasus PIV Nd:YLF laser with 2 heads in one unit. Each laser head had a peak energy level of 10 mJ at a wavelength of 527 nm while operating at 1 kHz. Each cavity was able to fire at up to 10 kHz but the energy dropped down to less than 2 mJ at 7 kHz and down to approximately 1 mJ at 10 kHz, per the manufacturer's specifications. It was found that when firing in single-image mode at 10 kHz, the light intensity was too low for the camera to capture useful images for flow imaging. The laser light was directed to the electrode via a Dantec Dynamics, Inc. high power light guiding arm. Once the beam exited the light arm, it was shaped and focused using Dantec Dynamics modular light sheet optics. The optics transformed the light beam into a

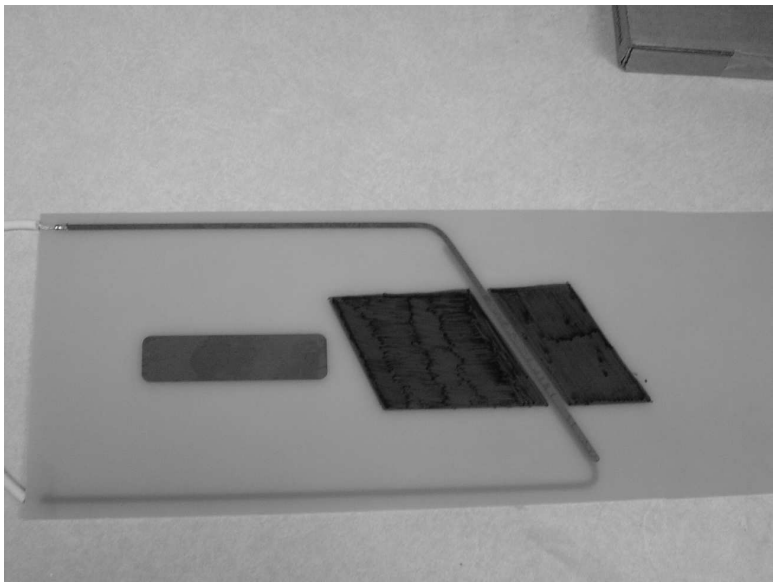

Figure 3.11: Electrode used to produce plasma with darkened area.

sheet and had a small adjustment for the focal length of the optics. It was found that the end of the laser light arm had to be approximately 43 *cm* above the electrode to have the light sheet focused at the correct point. For seed particles, a 1:1 mixture of propylene glycol and water was used.

3.5.2 Video Capture. To capture the seed particles illuminated by the laser, a high speed digital PCO.1600 14 bit CCD camera by Cooke Corp. was used, shown in Figure 3.16. The camera took images in double-frame mode with a 10 *ns* delay between exposures. The laser received a transistor to transistor logic (TTL) signal from the camera which made it fire at the same time as the first camera exposure. A Quantum Composer pulse generator sent the laser a second pulse 10 *ns* after the first to make it fire a second time, illuminating the particles for the second image. The camera had attached to it an adjustable bellows which allowed the focal length of the 102 *mm* Nikon lens to be adjusted at each location (discussed below). When the image was focused, the field of view was approximately 22 *mm* in the horizontal axis with a 4:3 image size ratio. The camera itself assigned that image to a 1600x1200 pixel image area. The camera assembly was affixed to a three-axis mount which

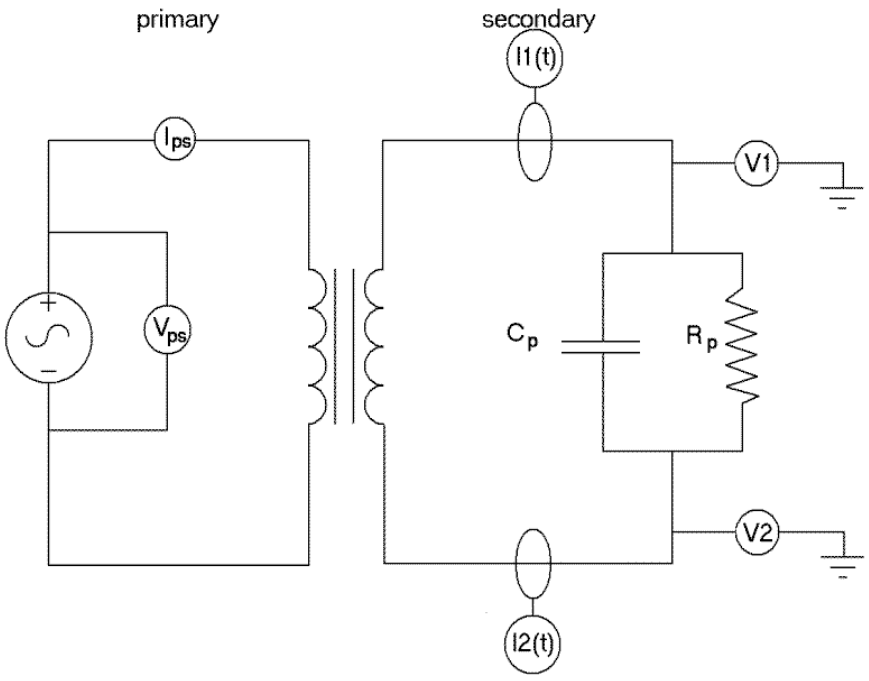

Figure 3.12: Schematic of plasma circuit.

allowed for vertical and horizontal movement. Images were taken at two separate camera orientations. The first orientation was perpendicular to the flow. The camera was positioned so that the focused image was coincident with the flow direction. In the other position, the camera was aligned so that it was sixty degrees from the flow direction and coincident to the electrode. This was necessary to take PIV images of the particles perpendicular to the electrode which was oriented thirty degrees from normal to the flow. Figure 3.17 shows a top view schematic of the two camera orientations in relation to the electrode.

3.5.3 Image Processing. The image pairs were imported to Dantec Dynamics Flow Manager software. To ensure the correlations reared proper values for velocity, and subsequently vorticity, the *field of view* was set to 22 *mm* and the image proportions were set to 4:3 (width:height). Also of importance was the time between images. As noted earlier, the delay of 10 *ns* needed to be set in the *acquisition control* setup. The horizontal and vertical size of each pixel as assigned by the camera also needed to be assigned in Flow Manager. For the PCO.1600 camera, the pixel size was

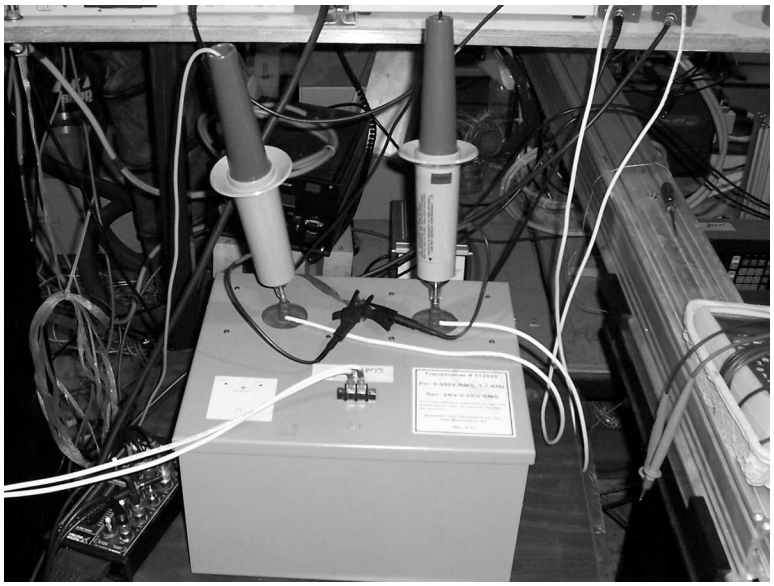

Figure 3.13: Transformer used to supply high voltage to electrode.

7.4 μm^2 x 7.4 μm^2. The *field of view* and *acquisition control* variables were assigned during the project setup prior to importing images. Failure to do this would result in erroneous correlations, requiring a re-importation of the images.

3.6 Data Acquisition

3.6.1 Instrumentation. Pressures were measured using two Druck differential pressure transducers, shown in Figure 3.18. Both transducers were LPM 9000 series differential transducers. One was a 0 - 0.2 inH_20d with a non-linearity of $\pm 0.1\%$ of the free stream best straight line approximation (FS BSL) and the other was a 0 - 0.8 inH_20d, also with a non-linearity of $\pm 0.1\%$ FS BSL. The 0.2 inH_2Od transducer required a 16 - 30 VDC input voltage while the 0.8 inH_20d required a 10 - 30 VDC input power. Each transducer was supplied power via separate DC power supplies both of which were set to 20 VDC. The former transducer had an output of 0 - 10 VDC while the latter had an output of 0 - 5 VDC. The 0.8 inH_2Od transducer was used with the boundary layer probe due to the flow velocity at the throat. The maximum velocity of the flow between the upper wall model and the electrode at

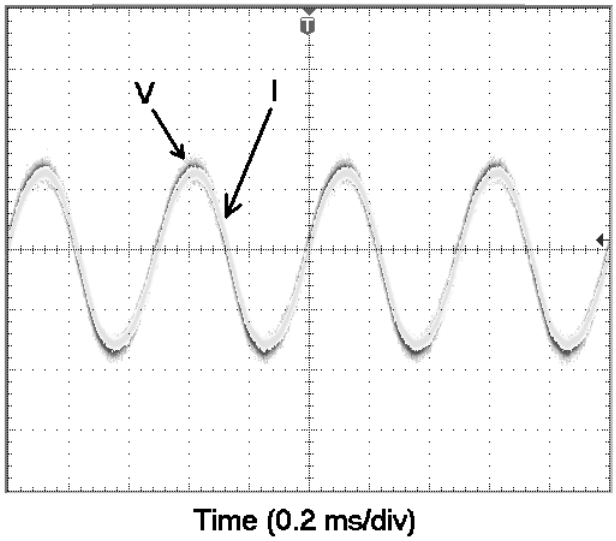

Figure 3.14: Power applied to pure resistor.

$Re_c \approx 100k$ using a variation of Bernoulli's equation shown in Equation (3.1) was approximately 30 ft/s.

$$66.103\sqrt{\Delta p\ (inH_2O)} = Vel\,(ft/sec) \tag{3.1}$$

This value was calculated using a measured total/static pressure difference of $\Delta p \approx 0.2H_20d$. To measure turbulence intensity, as well as another means of measuring the magnitude of the velocity at the throat, hot film anemometry was used. The anemometer used was a TSI IFA-100. Only one channel was necessary since a single-film probe was used. To calibrate a channel for use with a certain probe, each probe, probe support, and coaxial cable combination had to be calibrated. Since the process of hot film anemometry as described in Section 2.5 is focused on minute changes in resistance across the probe itself, the resistance of the probe support and connecting cable needed to be determined. The measurement of this value was accomplished by using a shorting plug across the two leads of the probe support. After measuring this value, it could be subtracted from the actual reading once the hot film probe was used. The procedure for calibrating the hot film probe and anemometer is included in Appendix D. The probes were calibrated using the TSI calibrator shown in Figure 3.19.

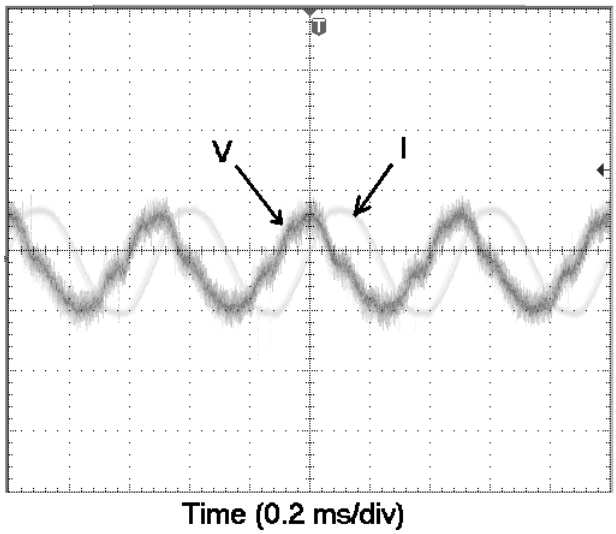

Figure 3.15: Power applied to electrode.

The calibration apparatus consisted of a pressure transducer, a nozzle, probe support and air jet, T-type thermocouple, and air supply valves. The calibrator was supplied compressed, dried air via an in-house supply. Atop the large cylinder in Figure 3.19 was a nozzle above which the film was centered. The total pressure probe was incorporated in the body of the calibrator and the other side of the transducer was open to ambient pressure. A supplied pressure versus velocity calibration curve was used to assign a value of velocity to a displayed voltage on the anemometer. The voltage versus velocity plot data for hot film anemometers will tend to be relatively linear with less linear curves near the operating limits. In order to determine the TI as well as the turbulence length scales with the anemometer, the voltage was converted to velocity data. The sampling rate of the anemometer by LabVIEW was 1000 samples per second. Each voltage sample was converted to velocity using the method outlined in Section 2.5. The 1000 velocity samples were then analyzed and the mean, standard deviation, and variance were found. The mean was then subtracted from each individual measurement to find the fluctuation of the signal. The fluctuation was then cross correlated with itself and the resulting data were plotted in order to calculate the length scale using Taylor's hypothesis. Taylor's hypothesis states that advection

Figure 3.16: High speed digital camera used with PIV.

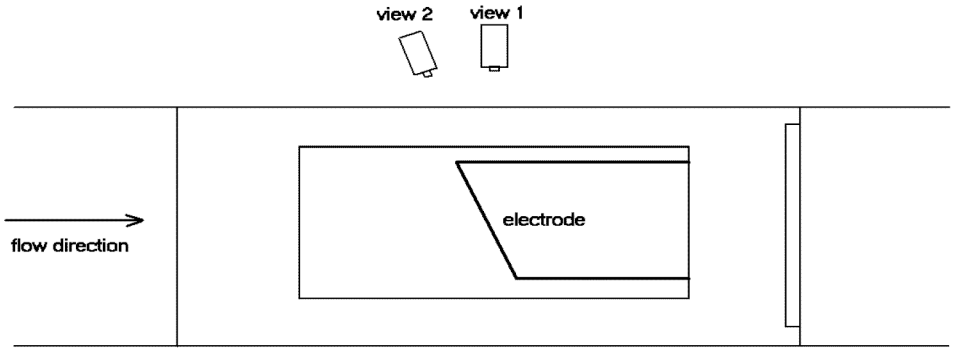

Figure 3.17: Camera orientations for PIV.

contributed by turbulent circulations themselves is small and therefore the advection of a field of turbulence past a fixed point can be taken to be entirely due to the mean flow [4]. A stipulation on the aforementioned hypothesis is that $u_e/U \ll 1$ where u_e is the eddy velocity and U is the mean flow velocity. Using this hypothesis and limitation the equation $t = x/U$, where t is time and x is the axial length, can be used to map the time domain to the length domain. The ratio of the standard deviation from the mean flow velocity and the mean flow velocity itself was defined as the TI. All calculations were performed using built in algorithms included with LabVIEW. Since the hot film used had only a single film, care had to be taken in positioning

Figure 3.18: Differential pressure transducers.

the film so that it was perpendicular to the flow. The alignment perpendicular to the flow ensured a proper velocity magnitude measurement in the axial direction. By virtue of the probe having a single film, only velocity magnitude in one axis could be measured.

3.7 Experimental Procedure

3.7.1 Data Collection Procedure. The sessions involving the use of PIV necessitated that the image be focused prior to collecting data, also the *field of view* had to be verified. Once the camera was set up appropriately, the wind tunnel and the upper wall suction were turned on and the free stream exit velocity was measured using a Kiel pitot probe. The Kiel probe measured differential pressure from which the velocity and subsequently the Re_c were determined. In order to get the desired velocity and Re_c the differential pressures were set to 0.021 inH_2Od for $Re_c \approx 50,000$, 0.047 inH_2Od for $Re_c \approx 75,000$, and 0.083 inH_2Od for $Re_c \approx 100,000$. Once the velocity was set, the upper wall suction was removed to ensure an attached boundary layer over the electrode surface. The plasma was energized and the correct power setting was adjusted using NIScope with LabVIEW. Once the power level was verified, the

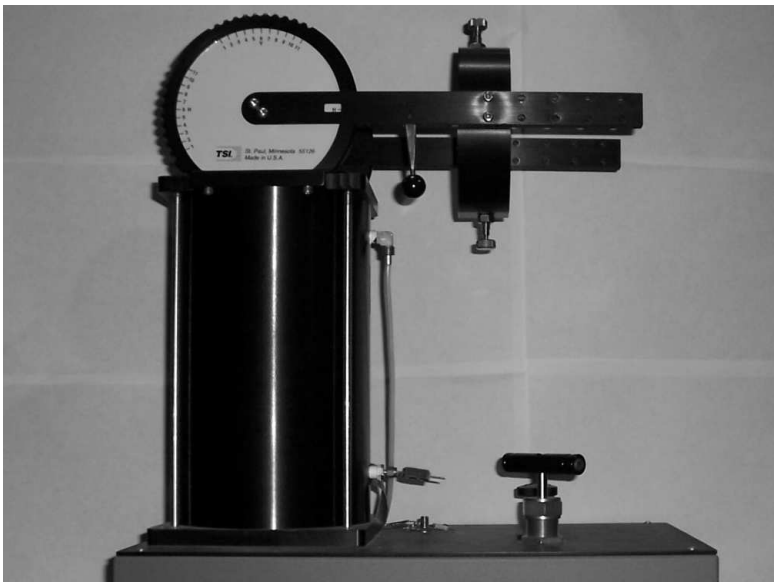

Figure 3.19: Apparatus used to calibrate a hot film anemometer.

upper wall suction was turned on and the seed particle generator was turned on. The power was set by observing the peak power that was recorded on the higher of the two electrodes, for three power settings this value was approximately 15 W, 20 W, and 25 W. The peak-to-peak powers were later checked visually using the waveforms in Appendix C and found to be approximately 22 W, 27 W, and 35 W. After the plasma was energized, the suction was turned on in an attempt to induce a boundary layer separation.

PIV utilizes small particles which are illuminated by the light energy from the laser. The particles were created by burning propylene glycol off of one of three heater elements and were approximately 0.5x10^{-3} mm in diameter. These small particles were injected into the flow prior to the flow leaving the conditioning plenum. Once the test section filled with seed particles, the PIV recording was initiated. After 80 image pairs were recorded the camera was stopped along with the seed particle generator. The plasma was de-energized and the next Re_c was set. The process was then repeated. The first set of 9 PIV trials were at low TI, with no turbulence generation apparatus in the flow. For high TI, a square bar mesh was inserted upstream of the

test section as shown in Figure 3.1. The square bars had 13 mm sides and the grid spacing was 59 mm on center. This resulted in a representative grid dimension of 13.4 mm for use with Roach's correlation discussed in Section 2.3. The data collection routine discussed above for the low TI cases was repeated for the high TI cases at the same Re_c. Once all data was collected with the camera image oriented parallel to the free stream flow axis, the camera was moved so the image would be aligned perpendicular to the long axis of the electrode. The above procedure was repeated again. Finally, to obtain data to compare with the PIV results, the laser arm and optics were removed and the micro-traverse and boundary layer probe were positioned 10.3 mm aft of the electrode, which consequently was one of the planes measured by the PIV correlations.

3.7.2 Test Matrix. Table 3.1 was completed to collect all the measurements described in section 3.7.1. The columns labeled Re_{ia}, where $i = 1, 2, 3$ refer to the measurements taken with high TI. The first three rows correspond to PIV images coincident to the stream, the second three rows correspond to PIV images perpendicular to the electrode, and the final row was completed using the boundary layer probe. The comparisons are included in the next section. Refer to Figure 3.17 for the orientation of either camera view.

Table 3.1: Data collection test matrix

Orientation	Input frequency	Input Voltage	Re_1	Re_2	Re_3	Re_{1a}	Re_{2a}	Re_{3a}
View 1	$3kHz$	$100V$	1a	2a	3a	4a	5a	6a
View 1	$3kHz$	$110V$	1b	2b	3b	4b	5b	6b
View 1	$3kHz$	$125V$	1c	2c	3c	4c	5c	6c
View 2	$3kHz$	$100V$	7a	8a	9a	10a	11a	12a
View 2	$3kHz$	$110V$	7b	8b	9b	10b	11b	12b
View 2	$3kHz$	$125V$	7c	8c	9c	10c	11c	12c
B.L. Probe	$3kHz$	$110V$	13b	14b	15b	-	-	-

IV. Results

The following sections compare the effects of the plasma on the separation layer. The comparisons are made by plotting three Re_c at a given power setting as well as three plasma power settings at a given Re_c. The data were measured at two turbulence intensities and two camera orientations for PIV. This section contains the plots corresponding to the 15 W case with varied Re_c and the $Re_c \approx 50k$ case with varied plasma power. The other four cases, the 20 W, 25 W, $Re_c \approx 75k$, and $Re_c \approx 100k$ cases, can be found in Appendix B. The results shown are the mean of eighty image pairs, thus showing time independent velocities. A sample of the standard deviation of the PIV data along with a comparison of PIV to boundary layer pitot probe data is examined. Also covered in this section is the visualization of the vortices which have been studied by Roth et al. [18]. The vorticity sections deal with two individual image pairs due to the time dependent nature of turbulent structures. That is, if it were desired to observe a vortex shedding, it must be seen instantaneously since it will not be a steady state phenomena. The vorticity was represented in two different manner. The first was by calculating the vorticity using the velocity vectors derived for a single image pair. The second representation used the same previous image pair, however the time averaged velocity was removed, leaving the fluctuation in vorticity.

Using Equations (2.1) and (2.2), the calculated resistance and capacitance had discontinuities due to the tangent term in the equations. The calculated resistance tended to infinity immediately prior to the quenching phase of the plasma as described by Enloe et al. [6]. Figure 4.1 shows the calculated resistance along with the associated voltage trace. Likewise, the capacitance has its discontinuities immediately prior to the local maxima of the current trace. Figure 4.2 shows the calculated capacitance on the same plot as the associated current trace. Note that where the capacitance tends to infinity, the current reaches a point of inflection. The aforementioned phenomena were not distinguishable to the naked eye, but was discussed as a point of note for possible future use in characterizing the plasma structure. As discussed in Section II,

Figures 4.1 and 4.2 show smoothed data. Recall, Figure 2.2 shows the raw current data with the wild oscillations near the extremum of the trace. It can be seen that once the calculated capacitance encounters the discontinuity just prior to the extremum, the current breaks down indicating the plasma has formed. It was determined that

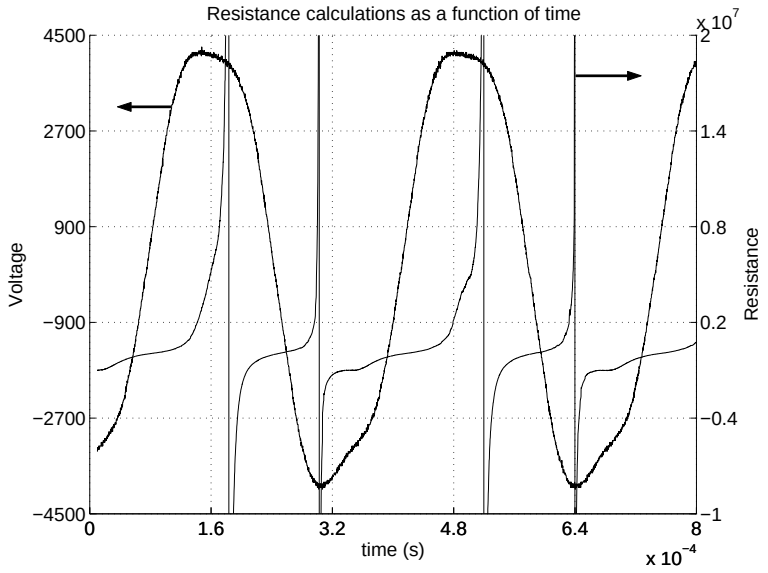

Figure 4.1: Resistance and voltage of plasma as a function of time.

the mean resistance and capacitance for the power setting displayed in Figures 4.1 and 4.2, were $5.16{\cdot}10^5\ \Omega$ and $1.05\ nF$, respectively. As discussed in Section 2.2 the flat plate assumption was deemed unreasonable. To show this, using the flat plate theory with the displacement being the thickness of the circuit card, the capacitance was found to be approximately 11 pF. This value of capacitance was two orders of magnitude different than the computed value based on the current and voltage of the plasma. A final note on power settings, the results contained herein are referenced to 15 W, 20 W, or 25 W. As discussed earlier, these levels were taken as the value of the upper peak of the voltage sweep on the oscilloscope emulator, NIScope. The actual peak-to-peak power these represented, were from approximately 20 W - 40 W.

All of the data presented in the following sections were derived using the data included in Appendix A, more specifically, the numerical value of the u and v compo-

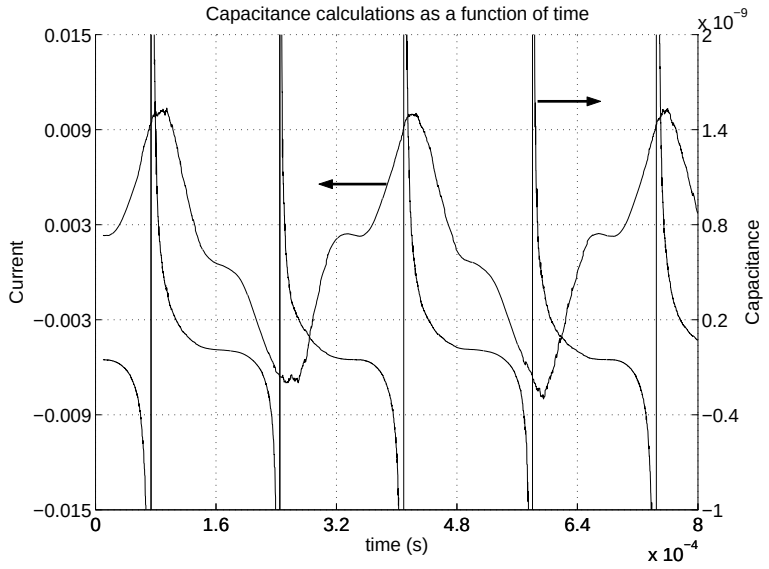

Figure 4.2: Capacitance and current of plasma as a function of time.

nents which made up each vector. Each vector plot shown in Appendix A is actually the mean of all eighty vector plots found using each individual set of image pairs. There is a marked difference between the figures using PIV data taken coincident to the free stream and the figures corresponding to PIV data taken normal to the electrode. The latter sets of vectors show what appears to be time independent turbulent structures. This was not actually the case however, but could be attributed to the large standard deviation of velocities over the entire set of image pairs for each setting. The standard deviation of the velocity data discussed here will be explained in the following sections.

4.1 Plasma Effect on Velocity Profile Normal to Free Stream

Shown in Figure 4.3 is the effect of plasma power at low TI on the velocity profile at a point 10.3 mm aft of the upper electrode. There was a very noticeable effect on the boundary layer velocity profile due to the use of plasma. Note that the majority of plots in this section have a non-dimensionalized displacement from the electrode on the ordinate. The actual distance from the electrode was normalized by the chord length of the simulated airfoil. In order to make the magnitude of the values from 0

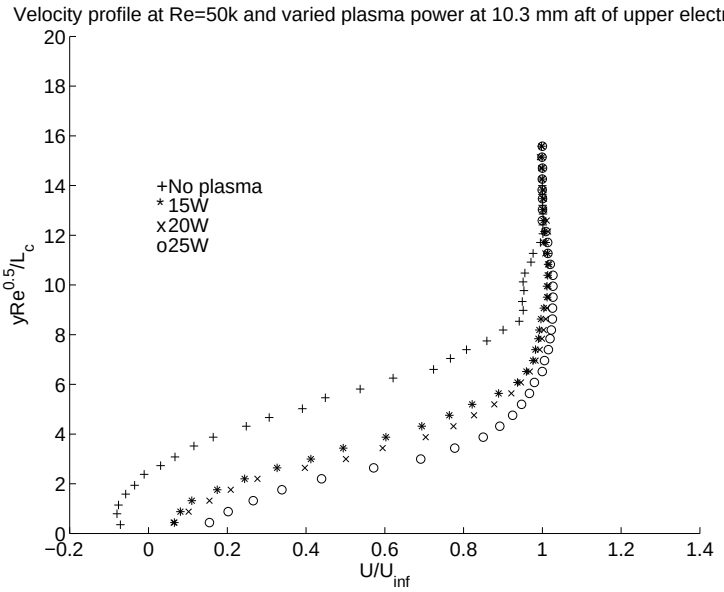

Figure 4.3: Velocity profiles, $Re \approx 50k$, varied power levels, low TI.

- 20 the result was multiplied by the square root of the Reynolds number based on modelled chord length (Re_c), thus mitigating some of the effects of the free stream Re_c on the results. The abscissa is a non-dimensionalized velocity. The actual velocity, U, derived via the PIV correlations was divided by the free-stream velocity, U_{inf}, which was the mean of the six values of U furthest from the wall. A result of this non-dimensionalization routine is that some values of non-dimensionalized velocity will be larger than unity. The TI measured via the hot film anemometer for the low TI cases was approximately 3.3%. The results shown in Figure 4.3 as well as the corresponding results in Figures B.1 and B.2 illustrate that plasma power had a profound effect on the velocity profile. The effect, however, was less profound on the boundary layer thickness. It is evident in Figure 4.3 and further shown in Figure 4.4 that there was almost no effect on boundary layer thickness between the three power settings. The effect on the boundary layer thickness was not, however one of the goals of this research. Note in Figure 4.4 that the ordinate was non-dimensionalized by $\delta_{.99}$, this axis definition is more commonly seen in plots of the boundary layer velocity profile and is included for comparison. The profiles for the 15 W and 20 W trials were

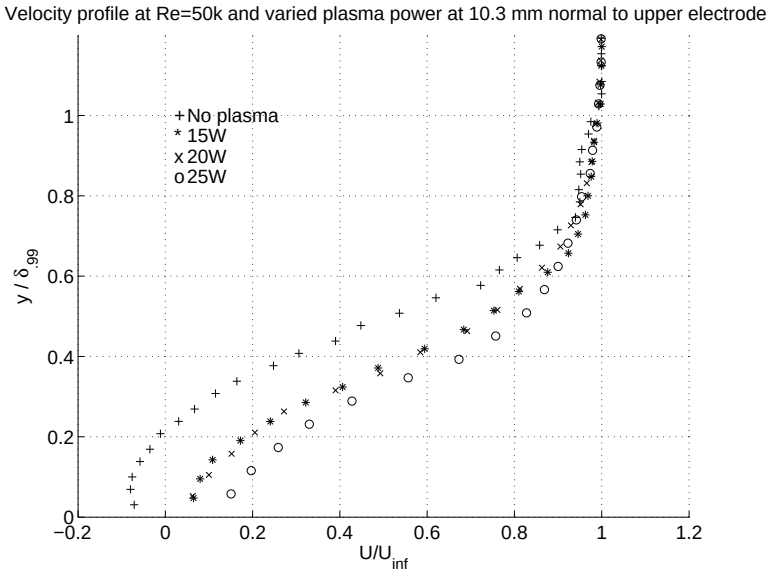

Figure 4.4: Boundary layer thickness, $Re \approx 50k$, varied power levels, low TI.

quite similar, the 25 W case showed a larger effect on the boundary layer thickness as compared to the no plasma case. This plot was the only one created with said axis definitions. The results obtained in the present study compared favorably to those obtained by Hultgren and Ashpis [8], however, as stated before only one electrode was used in a thirty degree off-axis configuration compared with a seven electrode array oriented normal to the flow utilized by Hultgren and Ashpis [8].

It should also be noted that the span and range of power settings used was small compared to those that which have been used by other experimenters [5, 17]. Recall the power settings in the present study were from approximately 20 - 40 W which are low due to only having one electrode and no matching circuits. For comparison, Chen [5] documented maximum powers from his impedance matched circuits of 587 W - 2804 W. The main reason such low power settings were used was due to the setbacks in time if a catastrophic failure were to occur. One such failure occurred with an input voltage from the power supply to the transformer of approximately 70 V at an input frequency of 10.7 kHz. The plasma arced to the electrically isolated boundary layer probe and back to the circuit card. Very soon thereafter the board

heated up and began smoldering. Burn through occurred where the voltage initially arced to the probe. A second burn through occurred near where the upper electrode first comes near the edge of the lower electrode. The frequency limitation found here was also noted by Wilkenson [23] who stated that he had frequent electrode failure at 6 kHz, furthermore at 10 kHz operation could only be done intermittently.

When the turbulence generating grid was positioned in the flow, approximately 55.25 cm upstream of the electrode, there was very little difference between the profiles with the plasma energized and that without the plasma. Figures 4.5, B.3, and B.4 show the velocity profiles with the high TI. The difference between Figures 4.3, B.1,

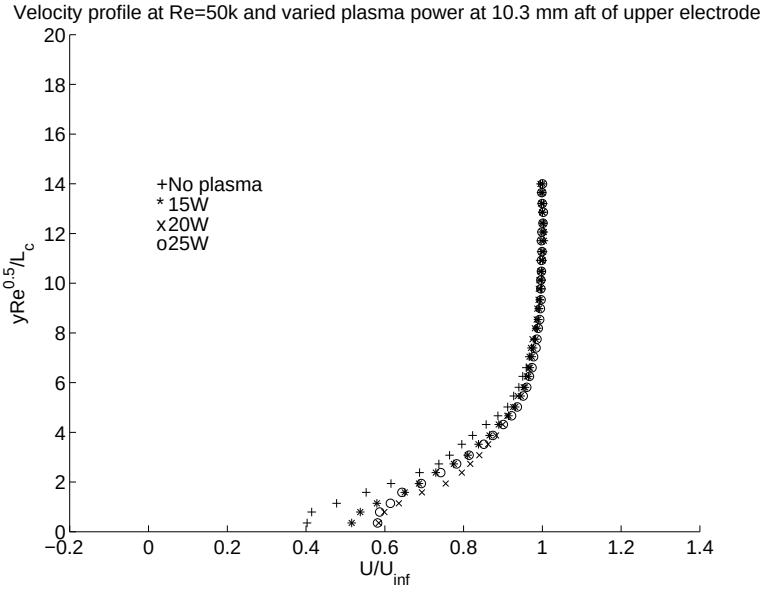

Figure 4.5: Velocity profiles, $Re \approx 50k$, varied power levels, high TI.

and B.2 and those mentioned above for the high TI cases, was simply the placement of a turbulence generating grid in the flow. Although there was a 3.3% TI present for the low TI cases, the velocity profiles more closely resembled a laminar boundary layer in the presence of an adverse pressure gradient. The high TI cases more closely resembled a turbulent boundary layer velocity profile whose non-dimensional velocity values reach unity at a position closer to the wall than the laminar case. For a given Re_c at high TI, an increase in the flow velocity was noted at the throat of the upper

wall geometry and electrode as compared to that with low TI. The increase in velocity was perhaps a result of the turbulent boundary layer growing faster than the low TI case and as such allowing a smaller area through which the flow could traverse.

The high TI measured with the hot-film anemometer was approximately 5.39%. This value caused some concern. To explain what may be happening, as the flow accelerates between the upper wall geometry and the plate, the turbulent flow structures would stretch and cause a lower turbulence intensity measurement. According Equation (2.7) the TI should have been measured at approximately 15.9%, without taking into account the magnitude of TI already present in the tunnel without the grid. The value of 15.9% is obviously larger than the actual value measured of 5.39%. In Equation (2.7), C_{turb} was a characteristic value of the geometry used (not to be confused with capacitance) whose value , as mentioned in Section 2.3, was 1.46. Of the other two variables, $x \approx 55.3\ cm$ was the distance from the grid to the measurement point, and $d \approx 1.34\ cm$ was the dimension of one of the sides of the square bars used.

To compare the effects of Re_c, all three values of Re_c for a given power setting were plotted together as shown in Figures 4.6, B.5, and B.6. Again, there was a noticeable difference in the near-wall velocities, but further into the flow, all three plots coincided. It can be seen that the theoretical no-slip condition does not seem to be present. This can be attributed to the large velocity gradient very near the wall immediately downstream of the plasma. Figures 4.6, B.5, and B.6 show adverse pressure gradients but no separated flow. As before, the high TI cases (referring to Figures 4.7, B.9, and B.10) show similar results as the low TI cases, but the regions where the near wall velocities are different are much smaller. For example, the plots for low TI and high TI are almost identical above a $\frac{y\sqrt{Re_c}}{L_c}$ value of approximately 6 but below that value the velocity profiles differ. The difference can be attributed to the type of boundary layer that is present. The low TI cases are measured in a laminar boundary layer whereas the high TI cases are taken in a turbulent boundary layer.

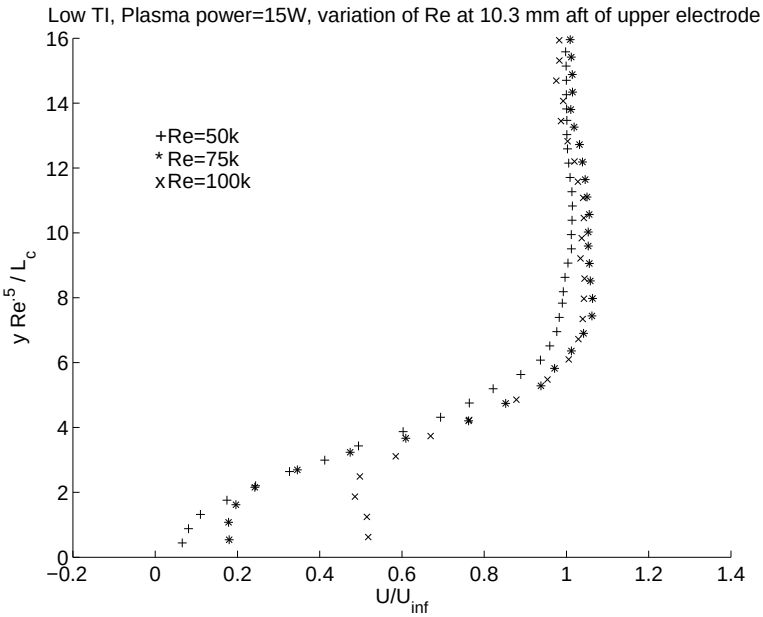

Figure 4.6: Velocity profiles, 15W power, varied Re, low TI.

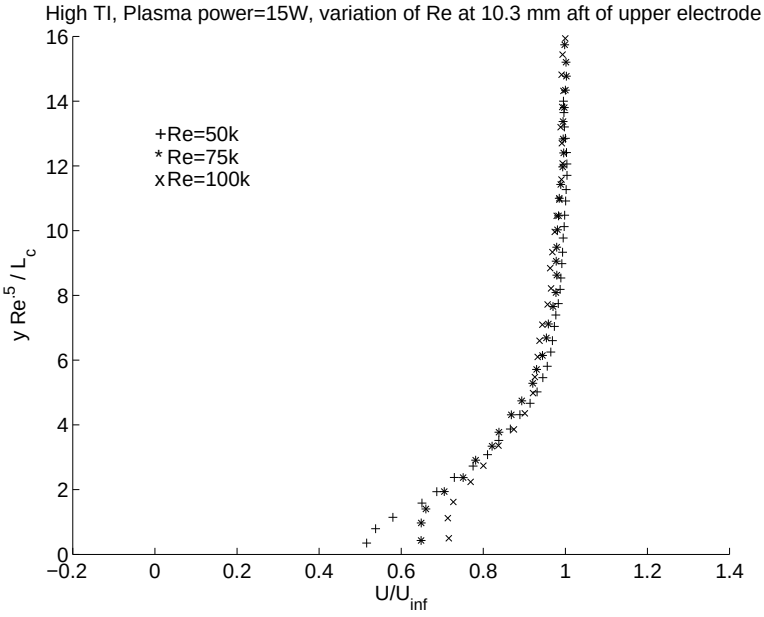

Figure 4.7: Velocity profiles, 15W power, varied Re, high TI.

The final set of plots dealing with the velocity profiles are those that compare the data obtained using a boundary layer pitot probe with the PIV data. Velocity profiles were taken with the boundary layer probe positioned approximately 10.3 mm

aft of the upper electrode. The velocity data was non-dimensionalized in the same way as the PIV data. Figures 4.8, B.7, and B.8 for the low TI cases, as well as Figures 4.9, B.11, and B.12, the high TI cases were created to display the results of the comparisons. For the high TI cases, all data sets comparing the PIV data to

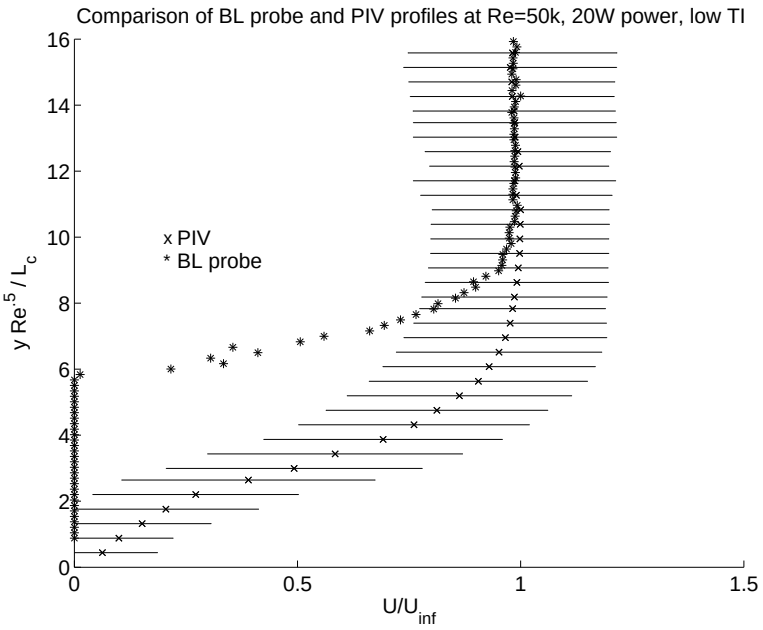

Figure 4.8: Comparison of BL probe and PIV data, $Re \approx 50k$, low TI.

the boundary layer probe data have good agreement. The low TI cases however, are not in agreement. The results presented for the boundary layer probe were confirmed using both the 0 - .8 inH_2Od and the 0 - .2 inH_2Od transducers. The verifications show there was a limitation in the ability of the particular boundary layer probe to measure the lower velocities near the wall, regardless of whether or not the plasma was energized. The limitation can be due to the length of plastic tubing running from the probe to the transducer, combined with the compressibility effects on the air. The results were also matched when the probe started at the upper end of the traverse and incremented down to the electrode as well as when started near the electrode and incremented up into the boundary layer and subsequent free stream. The final item displayed in Figures 4.8, B.7, B.8, 4.9, B.11, and B.12 comparing the boundary layer probe data to the PIV data were the error bars on the associated PIV data points.

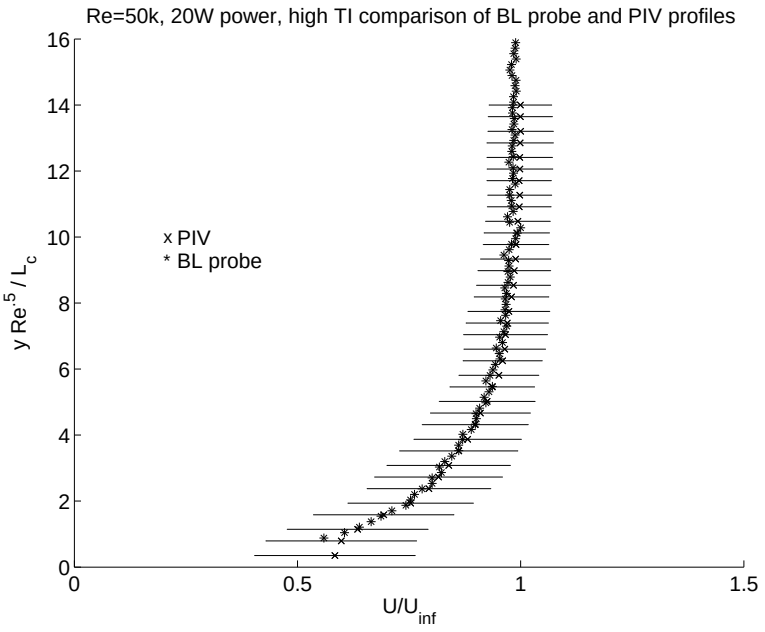

Figure 4.9: Comparison of BL probe and PIV data, $Re \approx 50k$, high TI.

The error bars represent the standard deviation of the U component of the velocity as determined by the PIV flow visualization software, FlowManager. The standard deviations are included to display the variation of the velocity at each point over the entire eighty image pair sequence.

4.2 Plasma Effect on Velocity Profile Normal to Electrode

The velocity profiles obtained in this section were done with the PIV camera and laser oriented normal to the electrode, labeled view 2 on Figure 3.17. Being that the laser sheet is out of the plane of the free stream flow, the number of particles imaged for the PIV auto-correlation were much fewer. The standard deviations were much larger and the resulting velocity data was not as organized as the previous section. Again, as in the previous section, there were eighty image pairs averaged to produce Figures 4.10 and 4.11. In these plots the velocity profiles were taken 10.3 mm normal to and aft of the upper electrode. The results in these figures can be compared to those shown in Figures B.7 and B.11 for the images taken normal

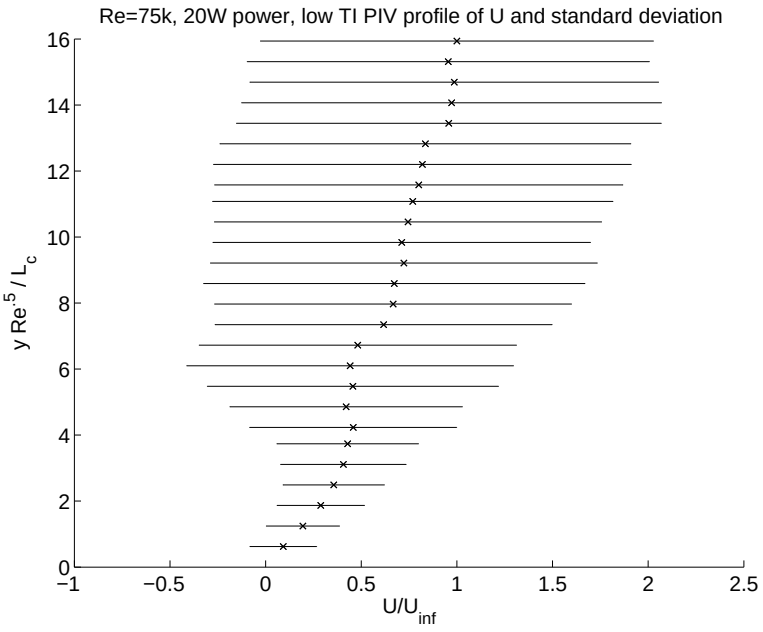

Figure 4.10: Velocity profile, $Re \approx 75k$, standard deviation of U, low TI.

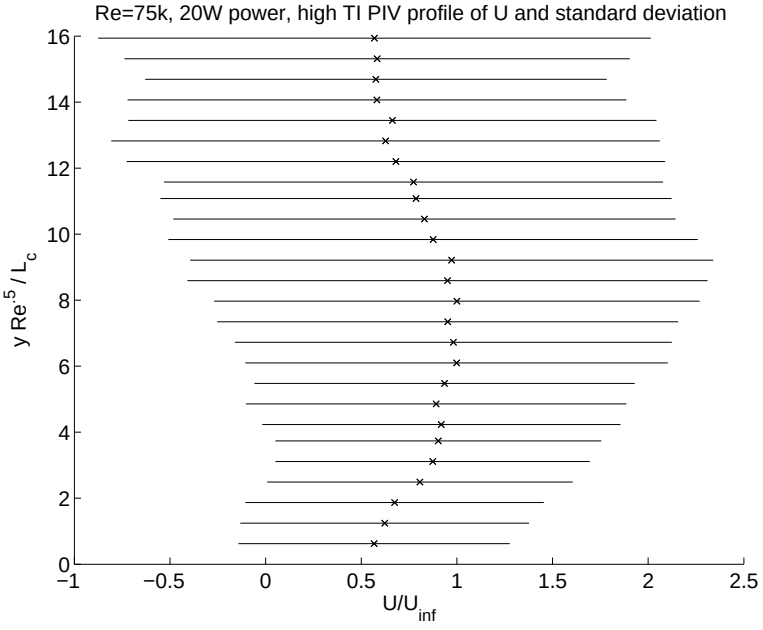

Figure 4.11: Velocity profile, $Re \approx 75k$, standard deviation of U, high TI.

to the flow. Note the change in the limits on the abscissa. There was an obvious increase in magnitude of the standard deviation of the velocity. The choice of the

cases corresponding to $Re_c \approx 75k$ were chosen because the other two cases had much larger standard deviations. Due to the larger standard deviation of velocity over the range of images, the results in this section are much less certain. They are included only to show general trends. The standard deviations tended to have the same trends as the values of the velocity, that is, as the velocity got larger, so too did the standard deviation. As a consequence of the unorganized profiles, the non-dimensionalization of the abscissa in the remaining plots in this section were done with the maximum value of U for each data set. Recall the previous section used the mean of the six values furthest from the wall. The data were collected at this orientation in an attempt to see if the vortex found to be generated normal to the electrode could be captured by the PIV.

The first set of comparisons in this section deal with Figures 4.12, B.13, and B.14. Noting that with the exception of the $20W$ and $25W$ data sets on Figure 4.12, all of the other data sets for low TI show adherence to the theoretical no slip condition at the wall. It is difficult to characterize what the plasma is doing to the near wall flow while oriented in this position. The corresponding plots for the high TI cases

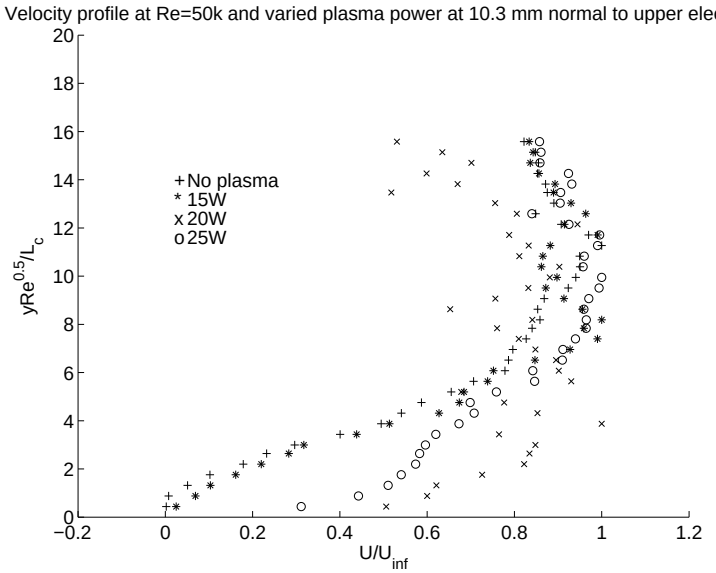

Figure 4.12: Velocity profiles, $Re \approx 50k$, varied power levels, low TI.

are shown in Figures 4.13, B.15, and B.16. One peculiar aspect is the fact that the location of maximum velocity in the normal direction occurs not near the plasma as shown by Jacob et al. [9] in the viscous sub-layer, but displaced a short amount above the plate at a value of $\frac{y\sqrt{Re}}{L_c} \approx 6$. Also of note, in the latter two plots, only the data set associated with the $25W$ case had a velocity that tended to $U/U_{inf} = 0$, the rest of the data sets, including those with no plasma, indicated a velocity very near the wall. When the data were compared with respect to changing Re_c as was done with

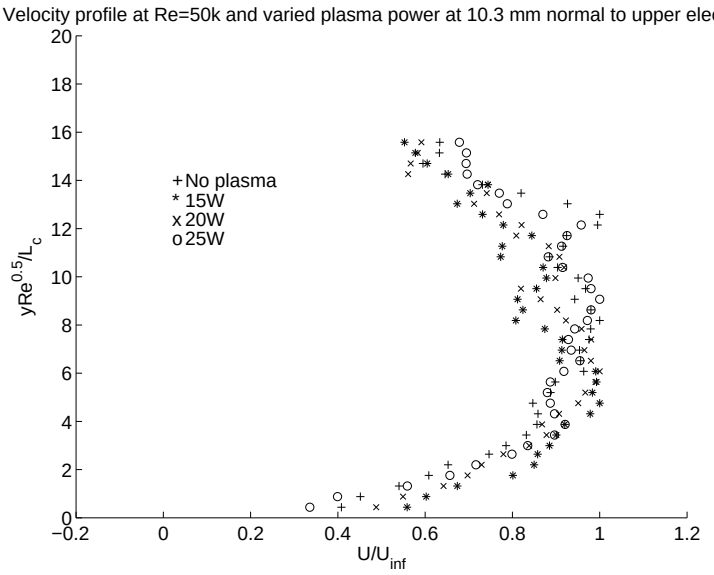

Figure 4.13: Velocity profiles, $Re \approx 50k$, varied power levels, high TI.

Figure 4.6 in the previous section, Figures 4.14, B.17, and B.18 show the effects, or lack thereof, of Re_c on the velocity profile in the normal direction to the electrode. At high TI, Figures 4.15, B.19, and B.20, show velocity profiles as a function of Re_c. In comparing the three plots, no generalizations can be made. Each velocity profile seems to follow a trend from one data point to the next, but those trends are not exhibited at the next plasma power setting. Due to the limitations dealing with getting PIV images at this orientation, it was difficult to ascertain trends which could be repeatable. The standard deviation of the velocity vectors were large enough to

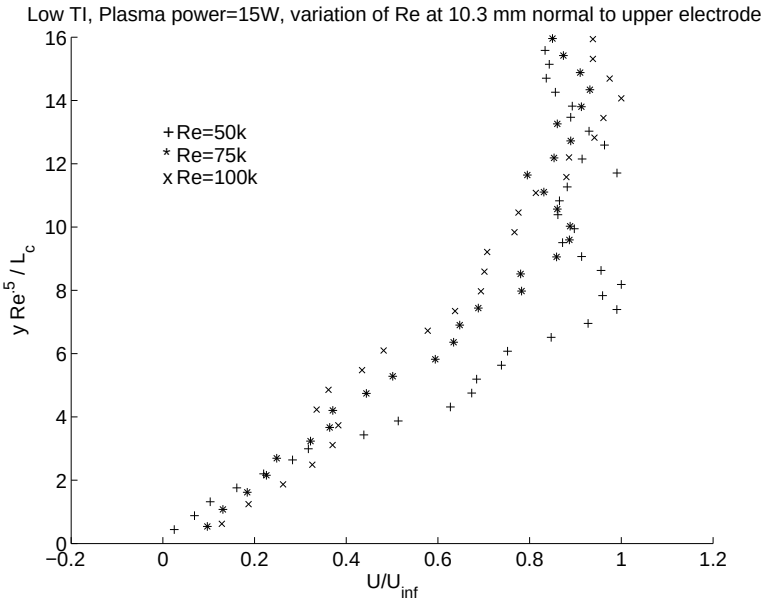

Figure 4.14: Velocity profiles, 15W power, varied Re, low TI.

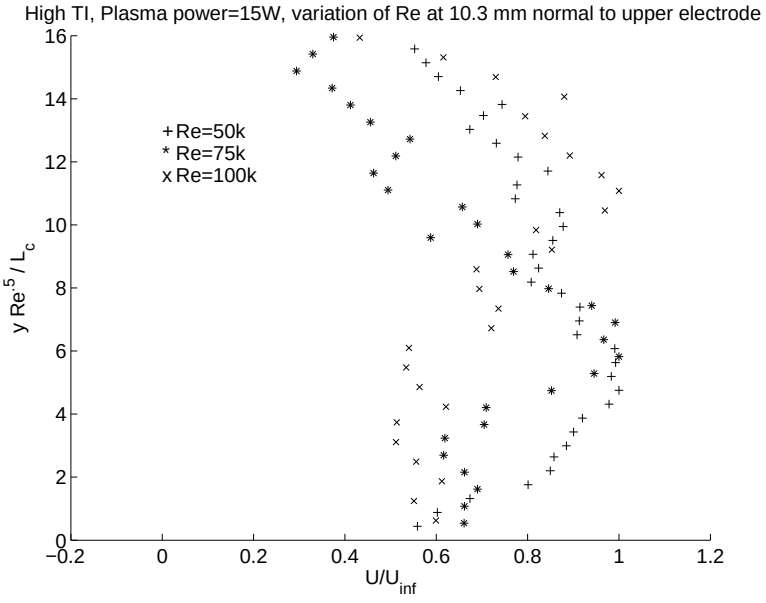

Figure 4.15: Velocity profiles, 15W power, varied Re, high TI.

allow for nearly any possible true profile. As such, very few, if any conclusions could be made from the data obtained normal to the electrode.

For the sake of comparison with other papers [21], the momentum thickness Reynolds number (Re_θ) was found for each setup. The results of the calculations are found in Appendix B. It was found that the results were of the same order of magnitude as found by Volino and Hultgren [21]. The only discrepancy was the negative value of Re_θ. The reason this value was negative was a result of the maximum velocity occurring below the upper end of the velocity profile. The fact that a large percentage of the velocity values were greater than unity, the sum over the entire profile resulted in a negative number.

4.3 Electrode Vorticity Generation

A method of visualizing the vortices that were produced by the plasma was necessary. Until now the only visualization noted was that done by Roth et al. [18] where they showed the effects of paraelectric body forces on titanium dioxide smoke streaks. The authors showed the effects of the plasma on flow running parallel to the electrodes. In the following figures, the flow is from left to right with the trailing edge of the upper electrode situated immediately left of the origin. The plasma is located on the bottom of the image from abscissa values of approximately 0 - 6. The numbers on the axes are simply place holders for the grid data to which the vorticity values were calculated. Since the representations chosen displayed the results as a function of grid point location, not the actual displacement, a superposition of the velocity profiles over the vorticity images was not accomplished. The vorticity images shown were taken on a plane parallel to the free stream located midway between outer edges of the electrode. The electrode itself can be thought of as starting from out of the image plane to the left and going into and through the image plane to the right. The angle between a line normal to the image plane and the electrode is thirty degrees.

The results presented in this section were produced in three different ways with the same results in terms of vorticity magnitude as well as representations of phenomena. Figures 4.16 and 4.18 display the vorticity calculated using two particular image pairs taken by PIV. Plotted are both velocity vectors at each data point as well as the

vorticity, which was defined as the curl of the velocity, or $\nabla \times \vec{V}$. Here both the del operator and the velocity vector are two dimensional, more specifically the vertical and horizontal axes. The second of the plots labeled Figures 4.17 and 4.19 are of the same data as the previous plots, however the averaged velocity field was removed. This was a method proposed by Liberzon et al. [13] to display the vorticity fluctuations, by removing what they termed background masking noise. It was decided the these latter plots were better representations of what was being sought. In looking at Figure 4.17, several phenomena were present. The main interaction of the boundary layer could be seen by the layer of low positive vorticity atop a region of strong negative vorticity. The largest gradients between strong positive and negative vorticity occur over the plasma whose location was previously described. Note that positive vorticity would be counter-clockwise on the included plots. Conversely, negative vorticity would rotate clockwise. Immediately aft of the plasma, approximately at the value of 10 on the abscissa, there begin alternating regions of positive and negative vorticity, eventually remaining positive. This could be thought of as a separated flow condition. At the upper edge of the boundary layer the strong negative and positive sheets of vorticity tend to dissipate downstream of the electrode. In visualizing the plasma during the PIV process, the particles could be seen as they were entrained by the plasma and accelerated along the plate. A short distance downstream of the plasma the particles would move up into the flow following a line that is thought to coincide with one normal to the field strength lines. This occurred at an angle of approximately thirty degrees from the wall starting at the point labelled 20 on the abscissa. It is here, where the plasma accelerates the air particles and then they move up into the flow, that a stable vortex should be found. In examining Figure 4.17 one such vortex appears to be present at the lower right corner of the image at approximately (44,6). Other prominent features are the two eddies which have shed from the flow. The eddy on the left has shed and is travelling almost vertically and the eddy on the right is heading down and to the right. In Figure 4.19, many of the same phenomena occur, however there was a large negative vorticity closer to the

plate than in the previous case. Some of the data extremely close to the plasma can be discarded due to the plasma itself illuminating the image during the video capture phase, something that will be addressed in the recommendations.

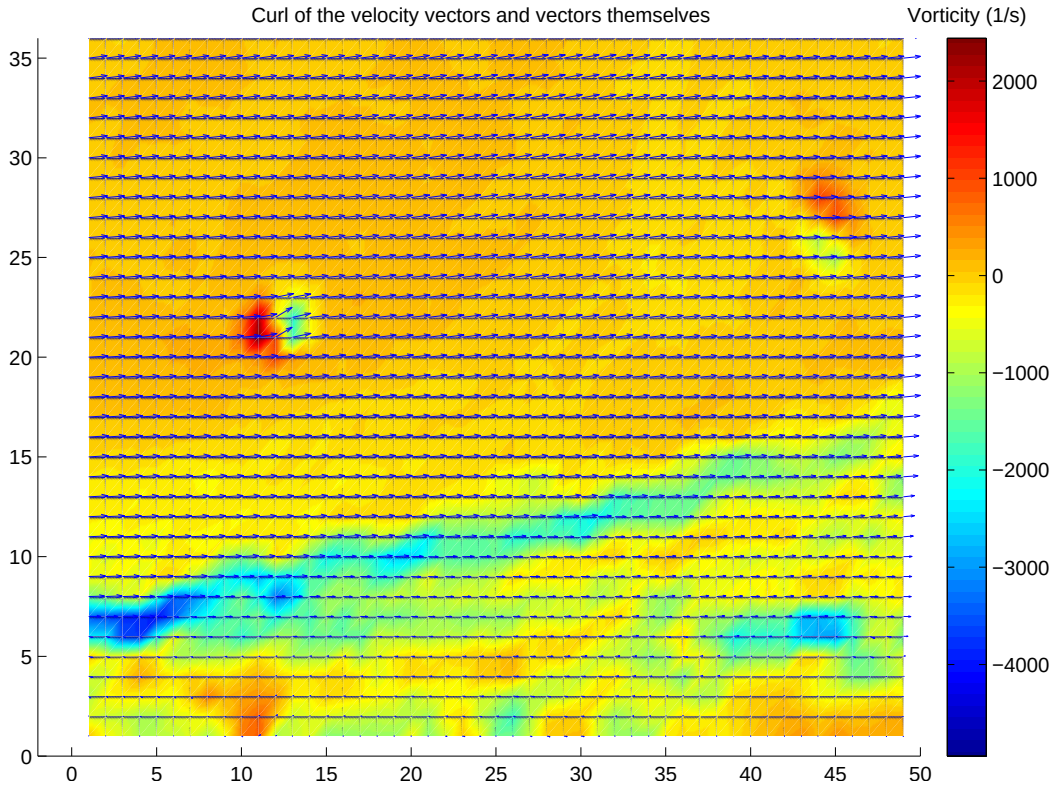

Figure 4.16: Vorticity of flow immediately aft of upper electrode, velocity vectors used to find curl.

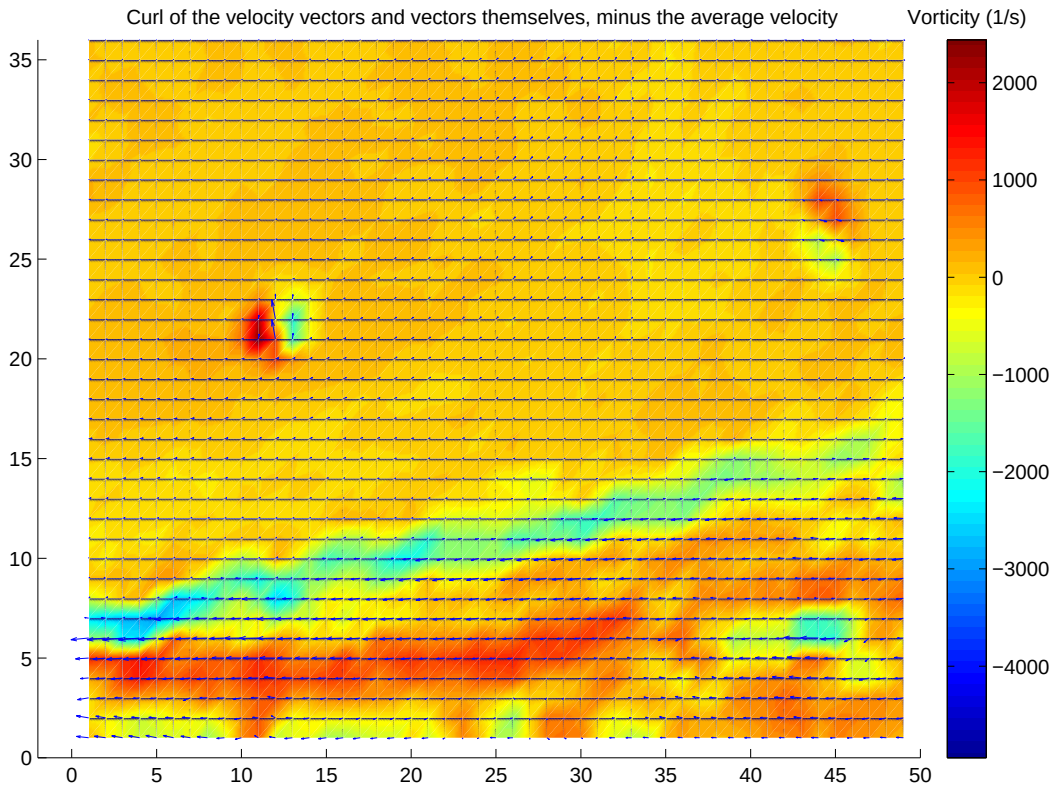

Figure 4.17: Vorticity of flow immediately aft of upper electrode, velocity vectors used to find curl.

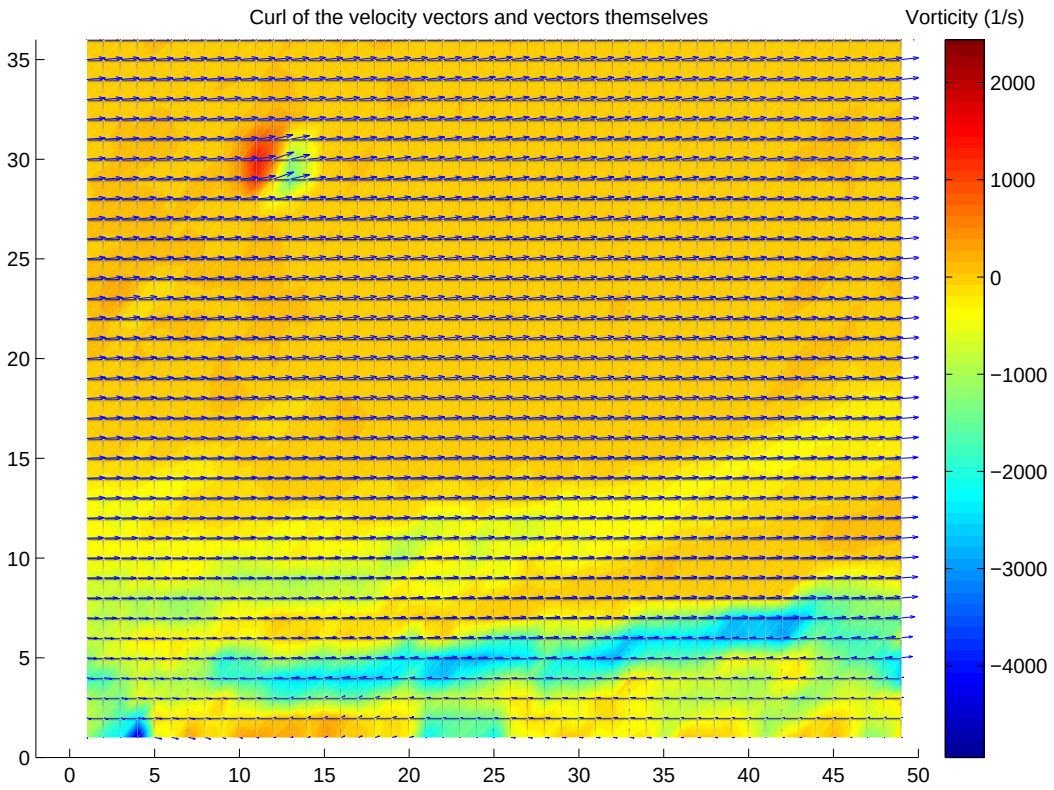

Figure 4.18: Vorticity of flow immediately aft of upper electrode, velocity vectors used to find curl.

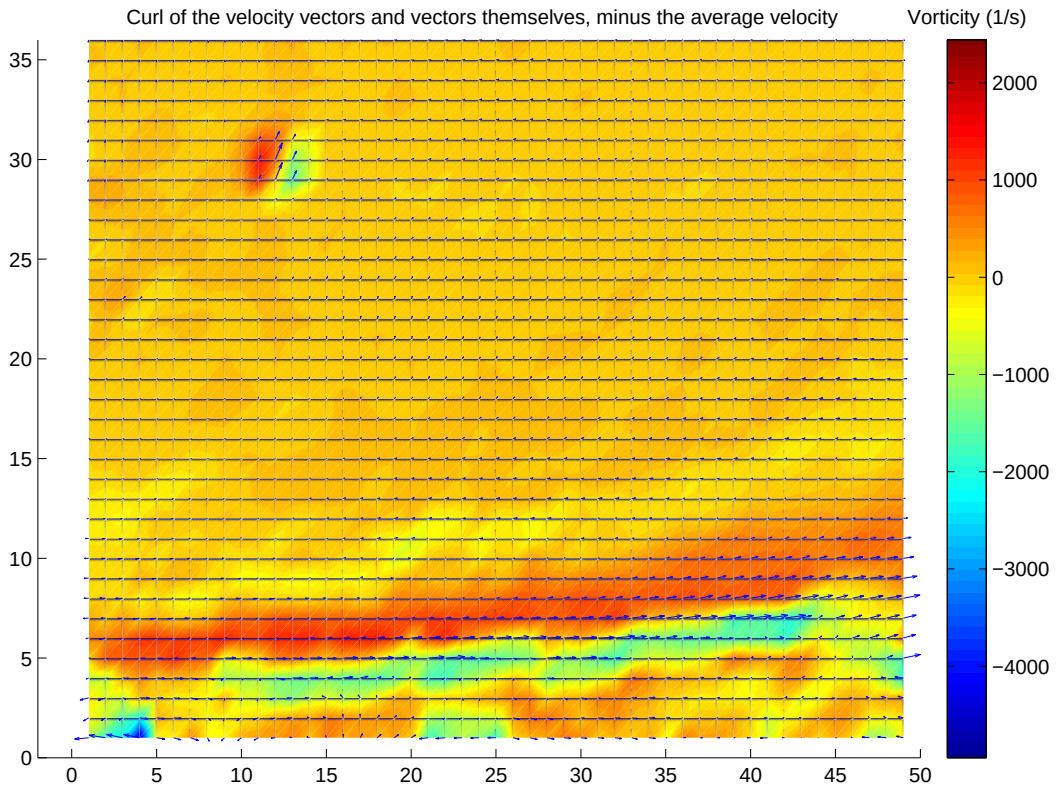

Figure 4.19: Vorticity of flow immediately aft of upper electrode, velocity vectors used to find curl.

V. Conclusions and Recommendations

The outcome of the data reduction was analyzed and the results have been compared to the objectives that were set forth in the Introduction. Further, recommendations have been presented for use in subsequent research efforts using the same facilities.

5.1 Stated Research Objectives

An objective of the research was to determine if there was a benefit to using a plasma generating electrode which was positioned thirty degrees from normal to the flow. It was found that the electrode used did in fact affect the boundary layer, causing the flow to remain attached in the presence of an adverse pressure gradient. The flow remained attached if the plasma was energized prior to inducing separation. The separation was verified by taking a baseline measurement with no plasma effects. The baseline data was then compared to the data taken with the plasma energized. The plasma was unable to reattach a boundary layer if the boundary layer was separated prior to the plasma being energized. The results shown for the electrode configuration studied here were comparable to those found by Hultgren and Ashpis [8] but the differences in setup configurations are too great to make concrete conclusions between the two. Another objective of the research was to study the turbulent vortex produced by the plasma and attempt to determine if it could remain stable as it convected down stream. There were vorticity images that do show a vortex immediately downstream of the electrode in the boundary layer. It is possible that the vortex may remain stable as it sheds away from the electrode, but the images must be time resolved at a higher rate than presented here to be conclusive. As a product of conducting the research, a data acquisition suite was created that could be utilized for subsequent research projects. The setup can be used with minimal adjustment for differing electrode configurations as well as changing the separation characteristics via an alteration or creation of a new geometry made from polystyrene foam.

5.2 Recommendations

The following recommendations are aimed at verifying the documented results and to assist in determining the benefit of the electrode orientation. First, the experiment should be reaccomplished with an electrode of similar length (and subsequently capacitance) oriented normal to the flow. The electrode should be positioned at the exact location where the PIV images were taken in relation to the axial distance from the throat of the upper wall geometry. This would ensure that the associated separation bubble is of the same size as was in this experiment. To make the setup up more robust, an effort should be put forth on maximizing the power applied to the single electrode. The use of impedance matching should be undertaken in order to increase the current applied to the plasma. A method for quantifying and scaling the upper wall suction should be realized. The suction should be scaled for each Re_c measured. This could account for the percentage of mass taken from the flow as it passes over the electrode. The end goal of this would be to make a separation region of the same height for each studied Re_c. This effect may already be mitigated partially by scaling the ordinate by $\sqrt{Re_c}$.

In order to study the turbulent structures, one would have to take PIV data at set time intervals. As the current arrangement is, the camera sends the laser a pulse at a time dictated by the camera software, it was not set by the operator. The timing was roughly 3 Hz but not verified. A time dependent study of the turbulent structures would have to be done. Also, the velocity at which the eddies shed would have to be determined and the PIV would have to take images fast enough to resolve those eddies as they shed.

Perhaps smoke injection very near the electrode much like Roth et al. [18] had done with the titanium dioxide, could better visualize the effects of electrode orientation. Consider if the smoke were released immediately upstream of the electrode. If once the plasma alters the flow carrying the smoke, the smoke travels down the electrode a short distance prior to being expelled in the flow direction, it would have to be

considered that it may have been entrained by a vortex with a component along the electrode. Comparisons could then be made between the effects of a typical electrode arrangement normal to the flow and an arrangement askew to the flow.

Appendix A. Velocity Vector Plots

The vector plots included in this section were taken with the laser sheet coincident with the flow as well as perpendicular to the electrode. Included here are samples of the velocity vector plots that were derived by the Flow Manager flow visualization software. It was these plots whose vector components were used to obtain the data presented in the previous sections. Included here are the profiles for $Re_c \approx 50k$ at the three power settings for both low and high turbulence intensity. The plots for the other values of Re_c were very similar with differing magnitudes where appropriate. The plasma location was identified by the set of symbols near the origin, the length of approximately 4 mm was the thickness of the lower electrode. The image was positioned such that the trailing edge of the upper electrode was located at the origin. The plasma formed at the trailing edge of the upper electrode and terminated near the trailing edge of the lower electrode, atop the circuit board.

A.1 Velocity Vector Plots Coincident to Free Stream

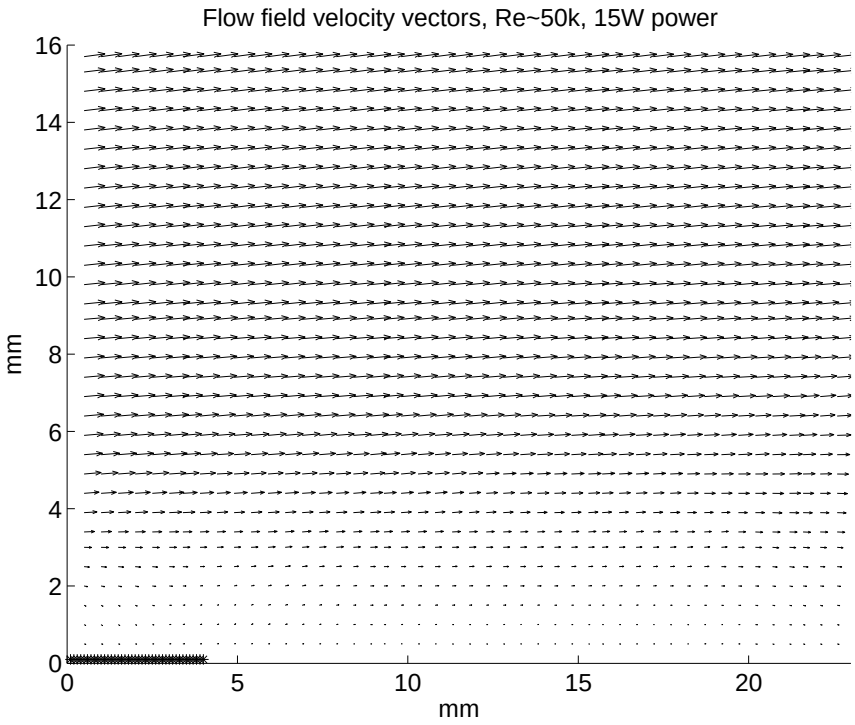

Figure A.1: Velocity vectors, $Re \approx 50k$, power level 15W, low TI, normal to flow.

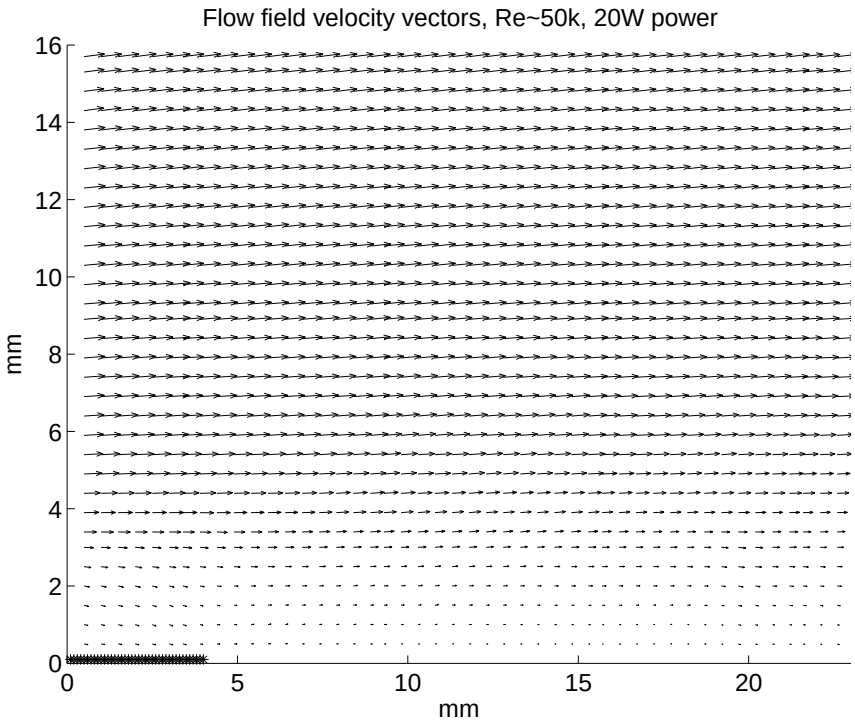

Figure A.2: Velocity vectors, $Re \approx 50k$, power level 20W, low TI, normal to flow.

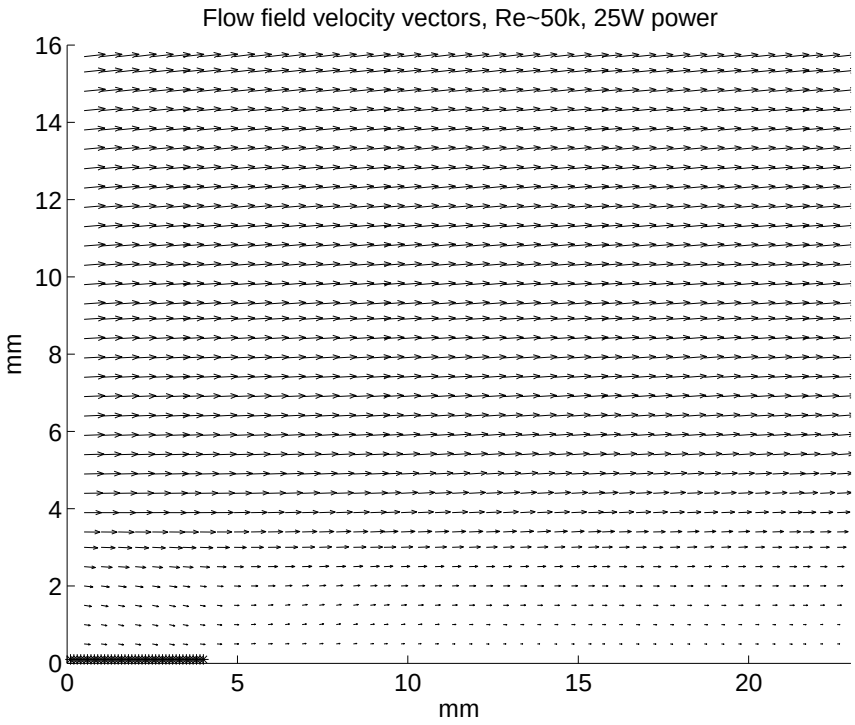

Figure A.3: Velocity vectors, $Re \approx 50k$, power level 25W, low TI, normal to flow.

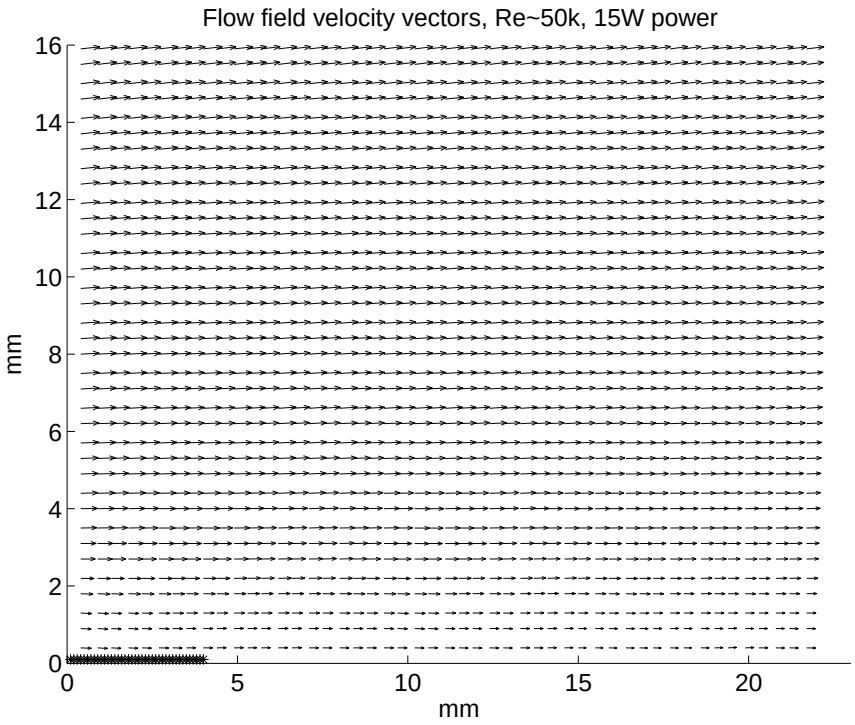

Figure A.4: Velocity vectors, $Re \approx 50k$, power level 15W, high TI, normal to flow.

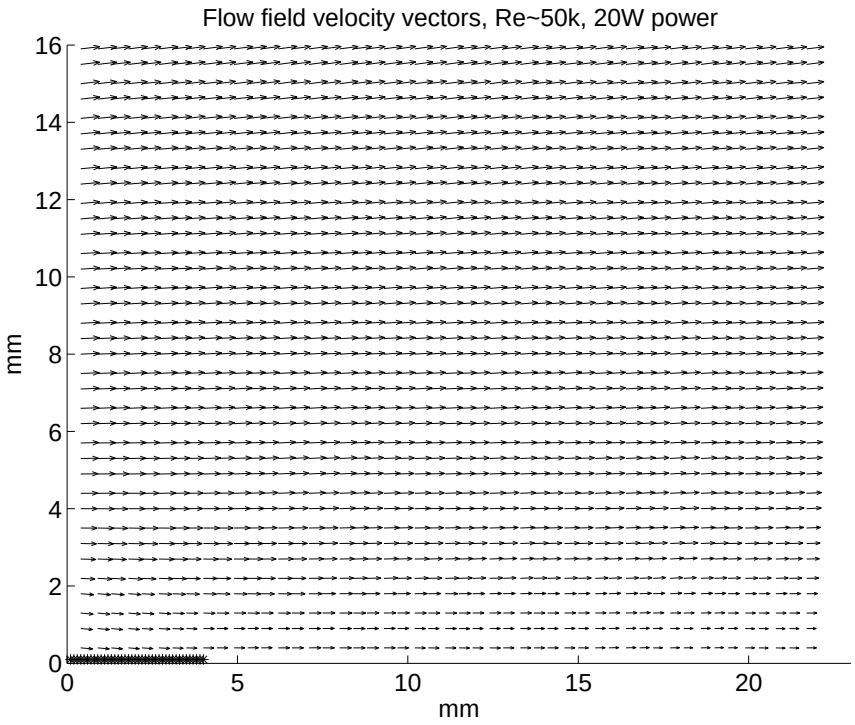

Figure A.5: Velocity vectors, $Re \approx 50k$, power level 20W, high TI, normal to flow.

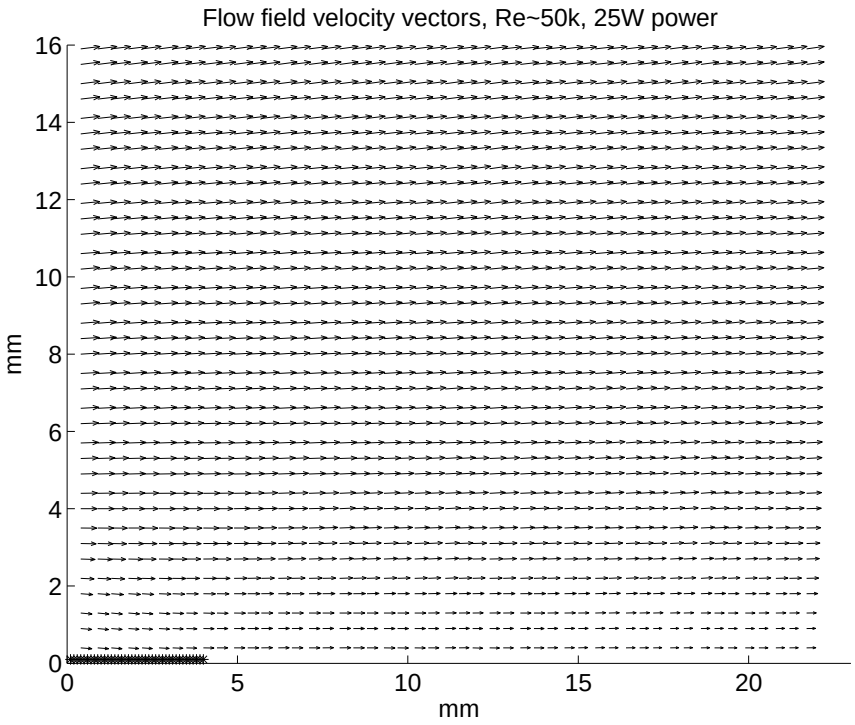

Figure A.6: Velocity vectors, $Re \approx 50k$, power level 25W, high TI, normal to flow.

A.2 Velocity Vector Plots Perpendicular to Electrode

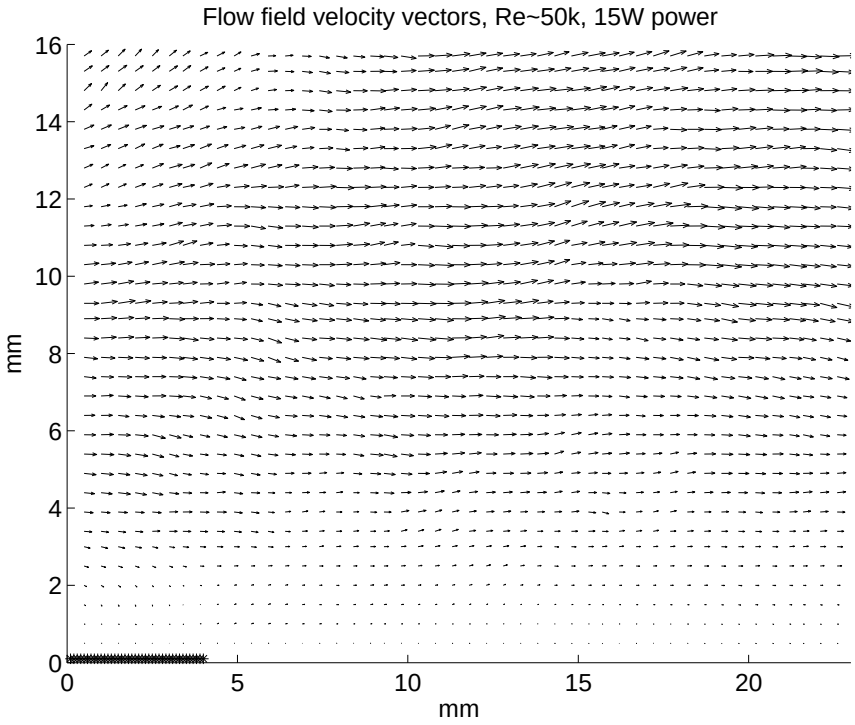

Figure A.7: Velocity vectors, $Re \approx 50k$, power level 15W, low TI, normal to electrode.

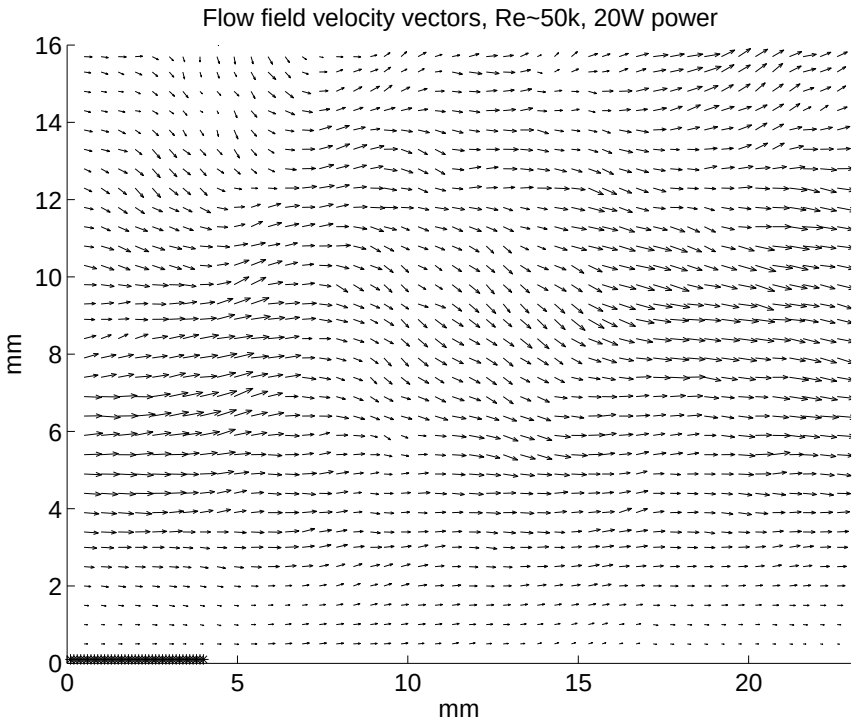

Figure A.8: Velocity vectors, $Re \approx 50k$, power level 20W, low TI, normal to electrode.

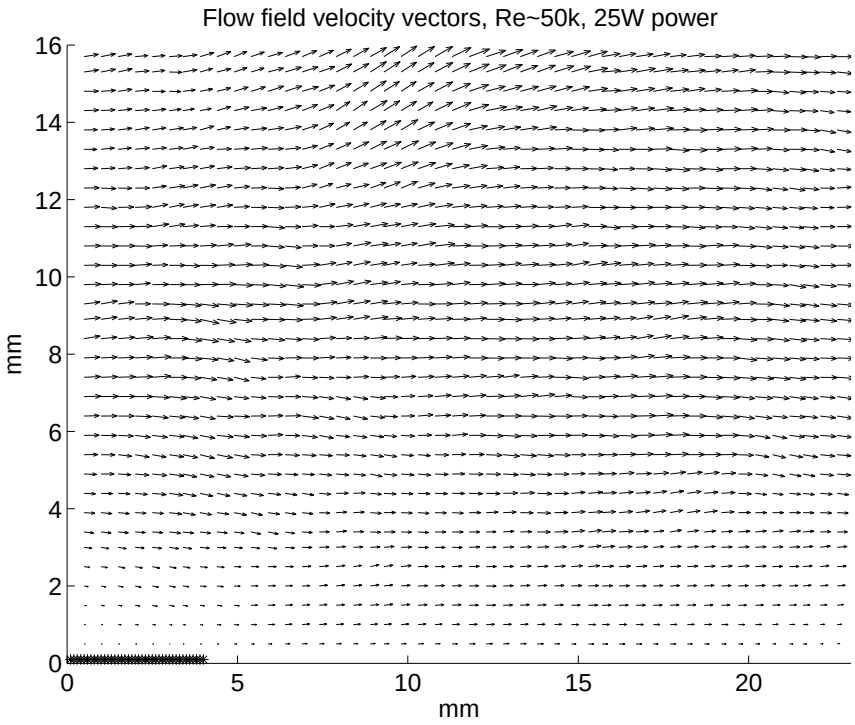

Figure A.9: Velocity vectors, $Re \approx 50k$, power level 25W, low TI, normal to electrode.

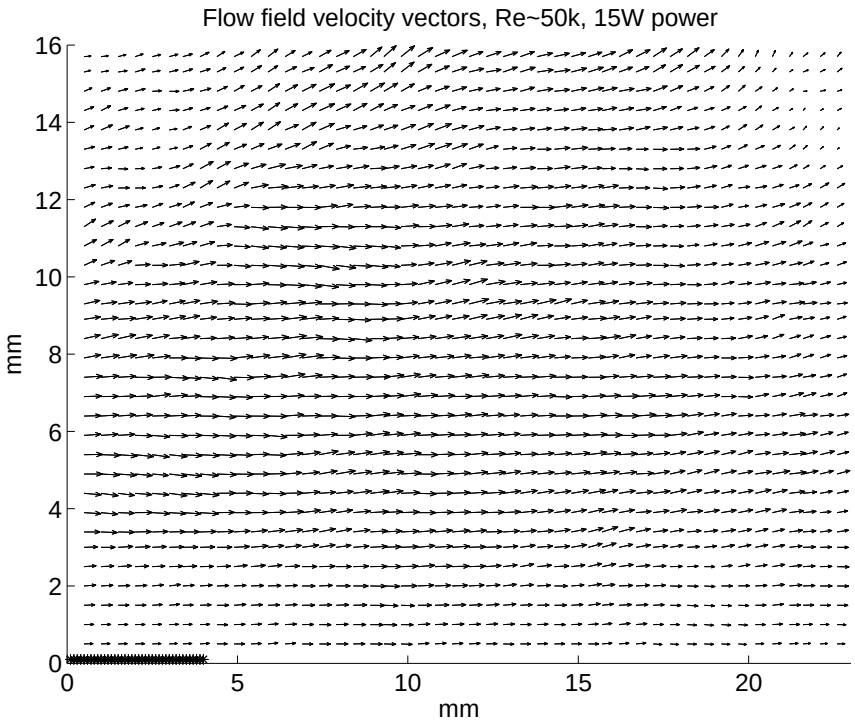

Figure A.10: Velocity vectors, $Re \approx 50k$, power level 15W, high TI, normal to electrode.

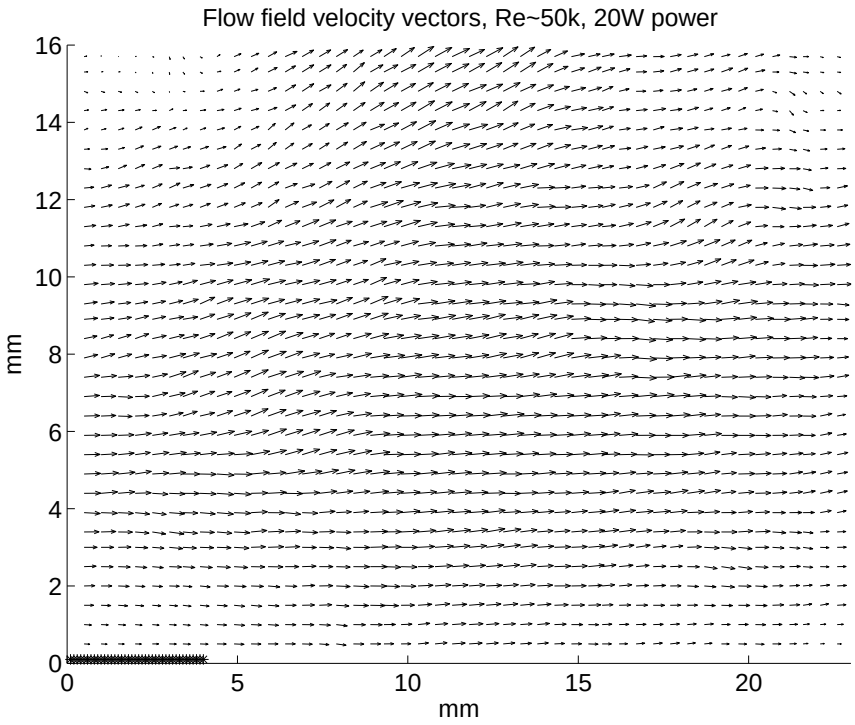

Figure A.11: Velocity vectors, $Re \approx 50k$, power level 20W, high TI, normal to electrode.

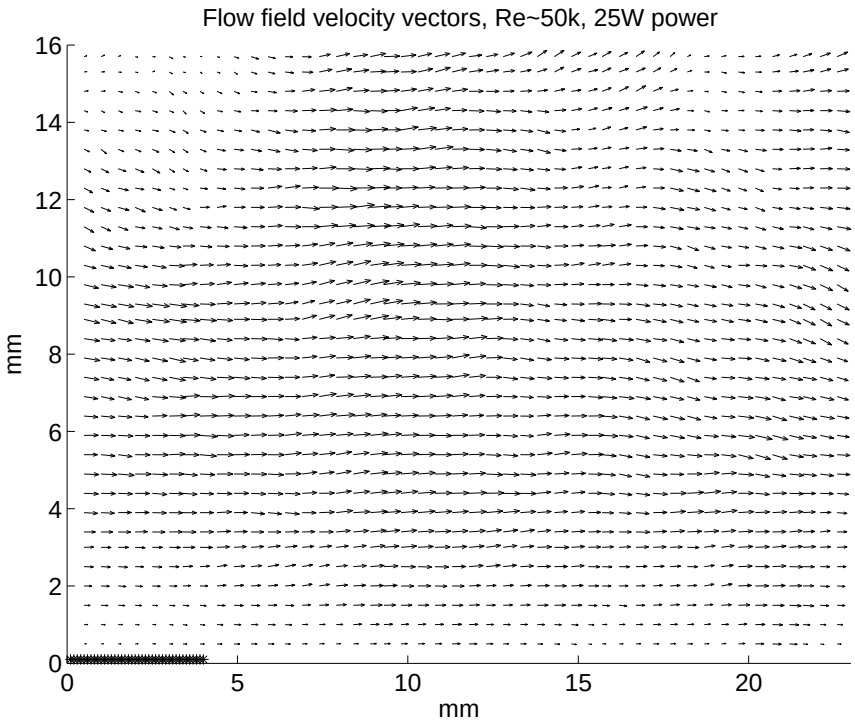

Figure A.12: Velocity vectors, $Re \approx 50k$, power level 25W, high TI, normal to electrode.

Appendix B. Velocity Profiles and Reynolds Number Calculations

The velocity profile plots in sections B.1 and B.2 are a continuation of the material presented in Section IV. The sections are divided up by how the PIV camera images were oriented, then by the turbulence level or power setting. The method used to determine Re_θ for each run at a given plasma power and Re_c are shown in Section B.3 using Equations B.1 and B.2.

B.1 Velocity Profiles Normal to Free Stream

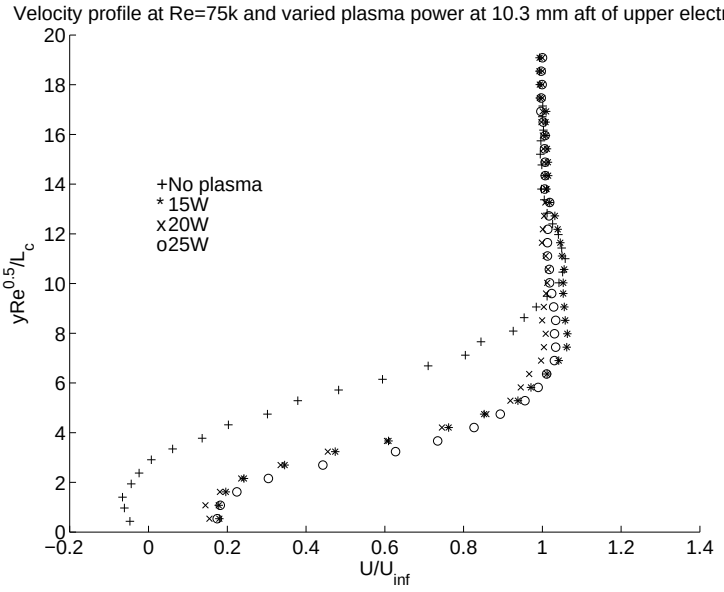

Figure B.1: Velocity profiles, $Re \approx 75k$, varied power levels, low TI.

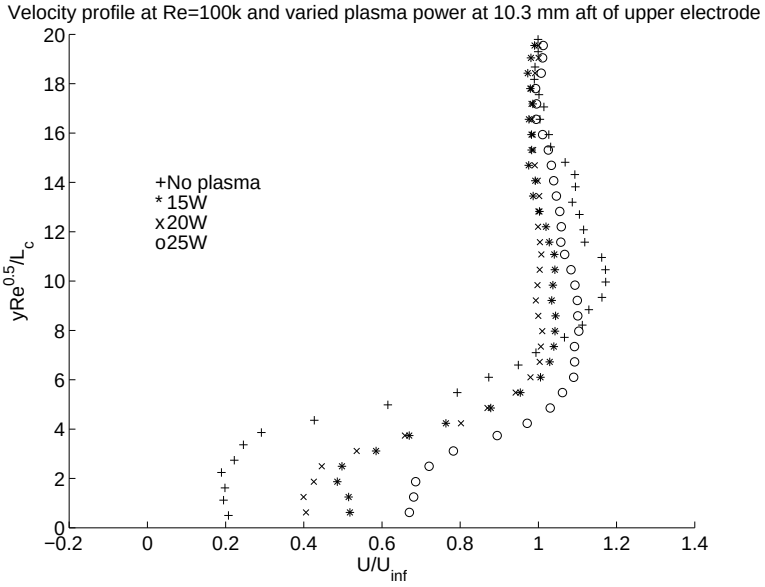

Figure B.2: Velocity profiles, $Re \approx 100k$, varied power levels, low TI.

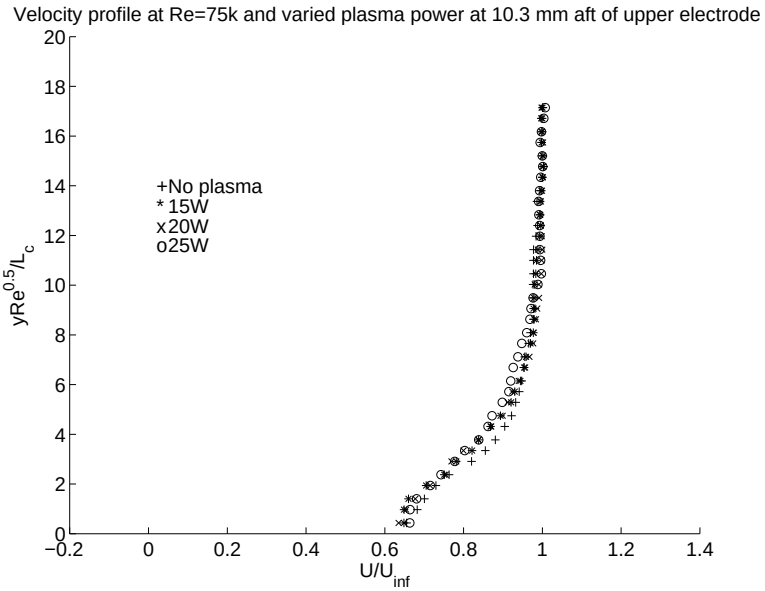

Figure B.3: Velocity profiles, $Re \approx 75k$, varied power levels, high TI.

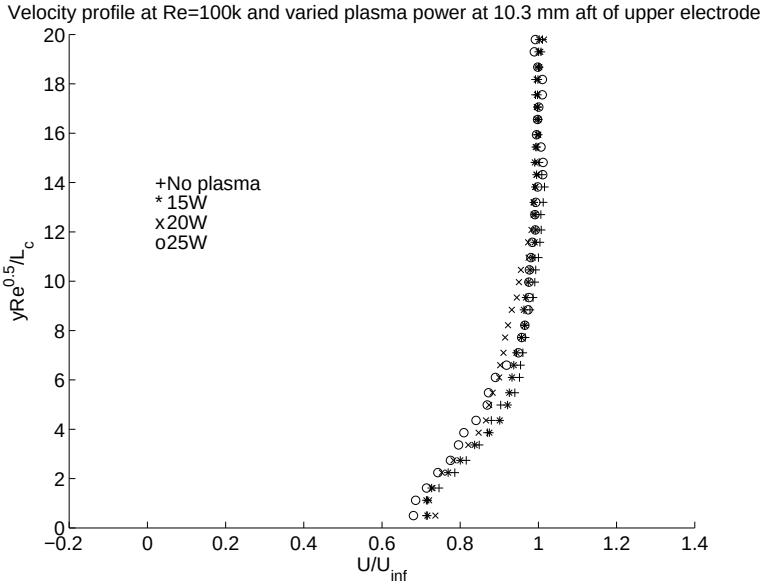

Figure B.4: Velocity profiles, $Re \approx 100k$, varied power levels, high TI.

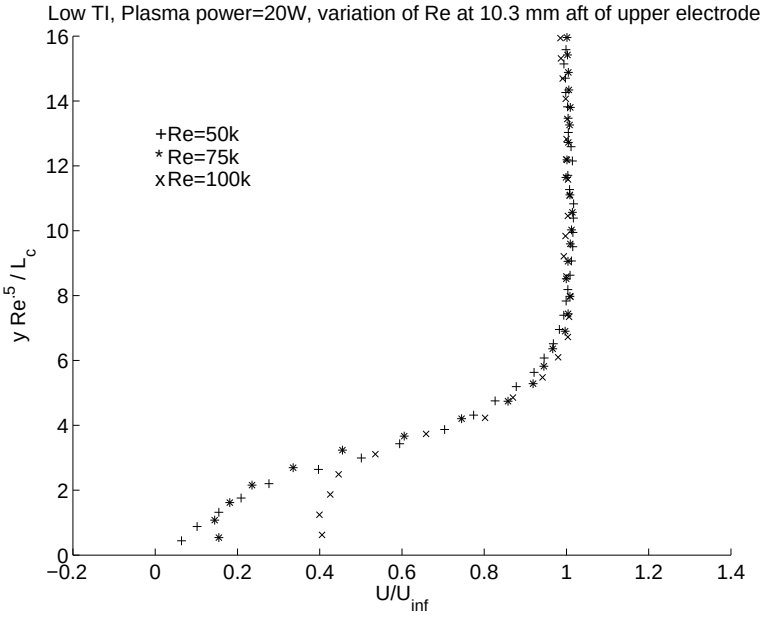

Figure B.5: Velocity profiles, 20W power, varied Re, low TI.

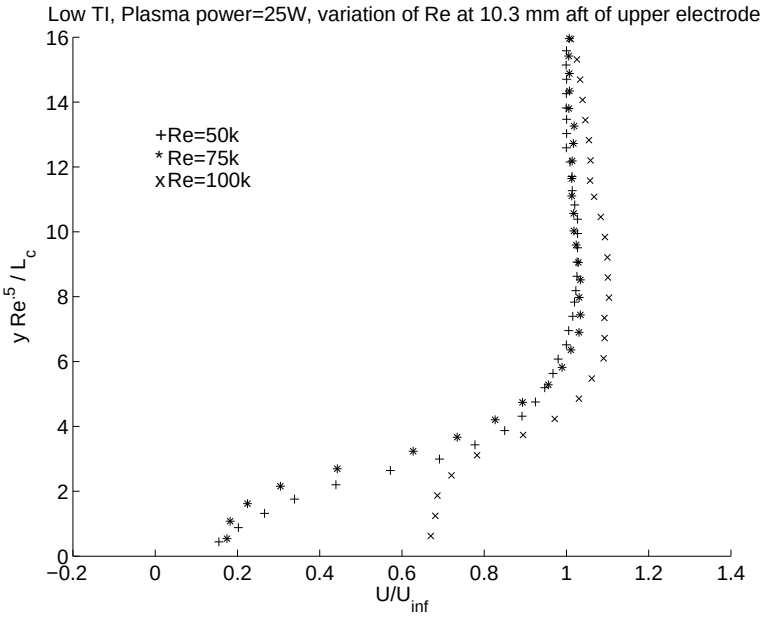

Figure B.6: Velocity profiles, 25W power, varied Re, low TI.

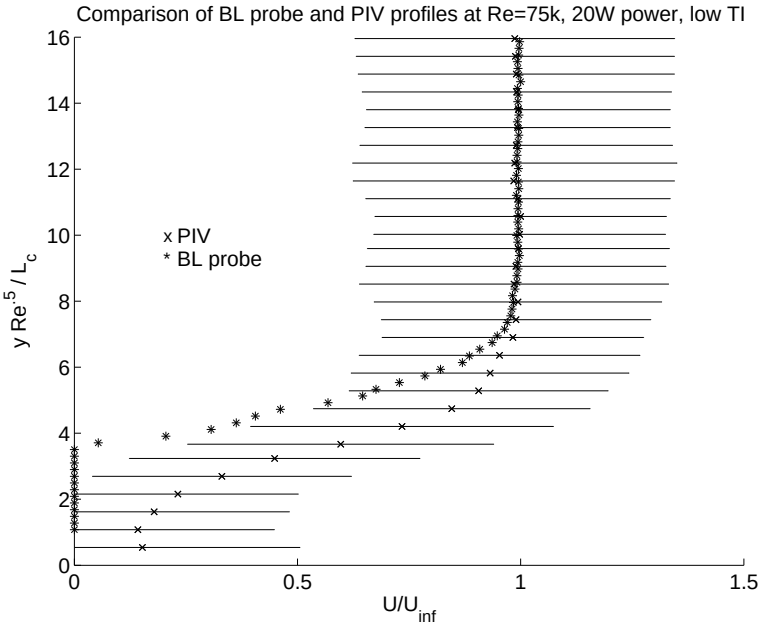

Figure B.7: Comparison of BL probe and PIV data, $Re \approx 75k$, low TI.

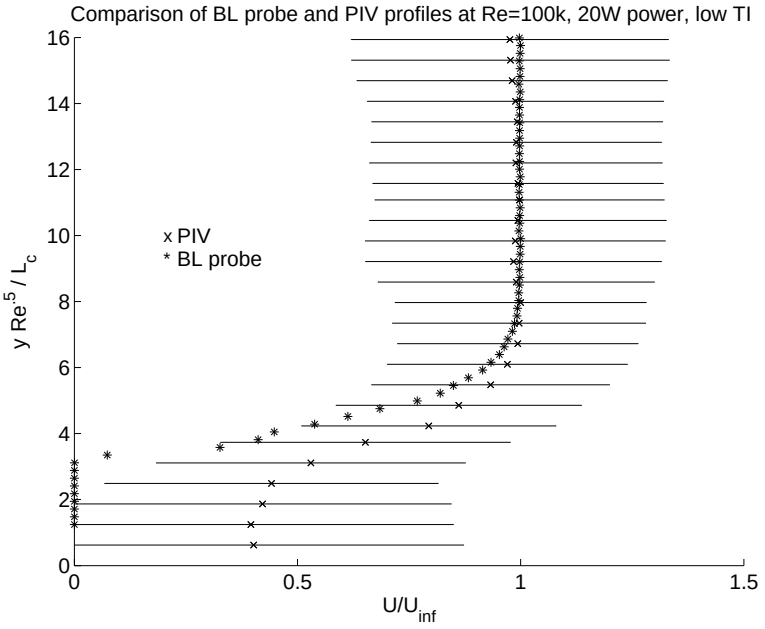

Figure B.8: Comparison of BL probe and PIV data, $Re \approx 100k$, low TI.

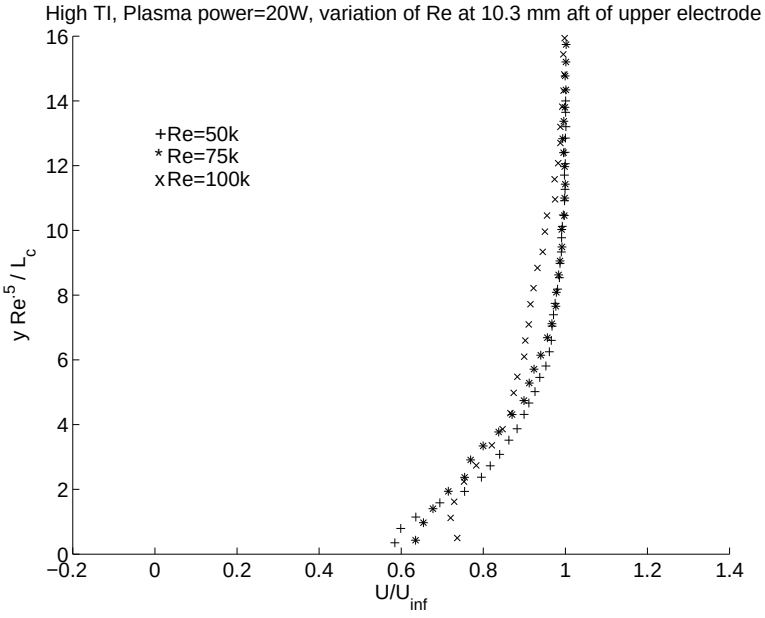

Figure B.9: Velocity profiles, 20W power, varied Re, high TI.

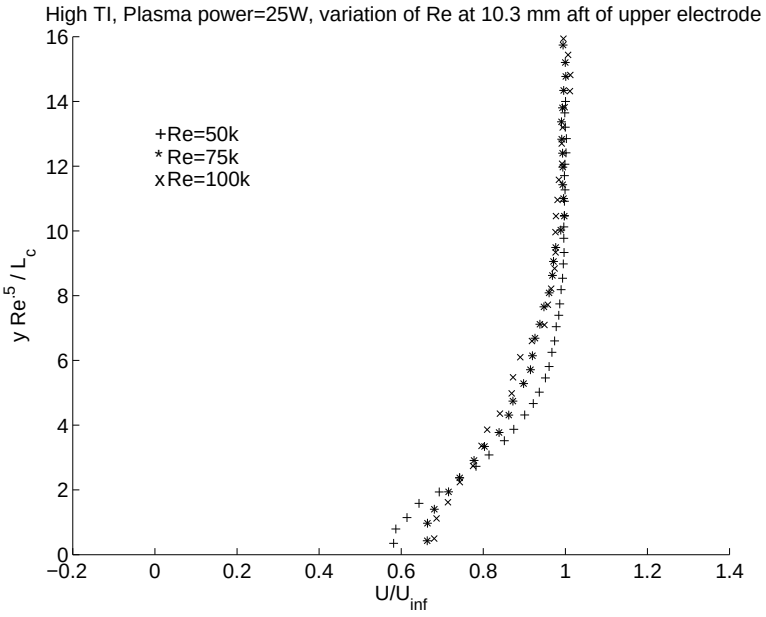

Figure B.10: Velocity profiles, 25W power, varied Re, high TI.

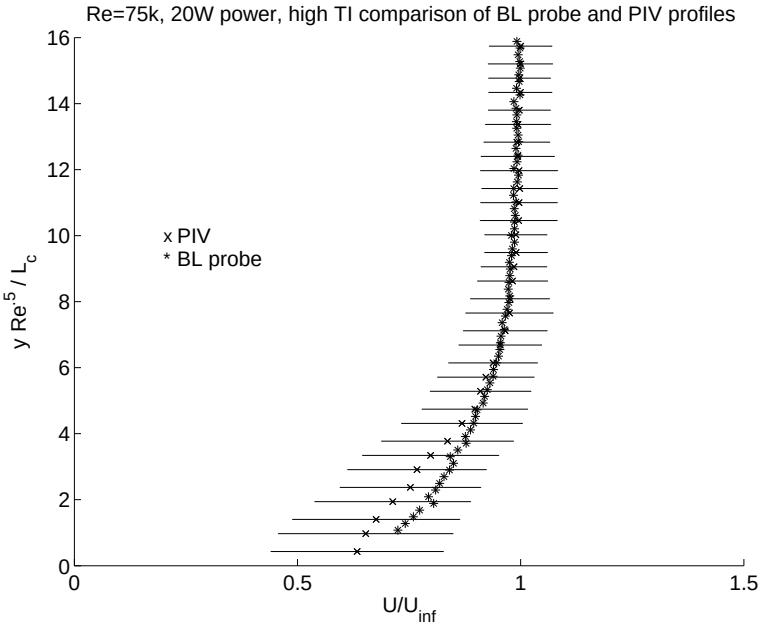

Figure B.11: Comparison of BL probe and PIV data, $Re \approx 75k$, high TI.

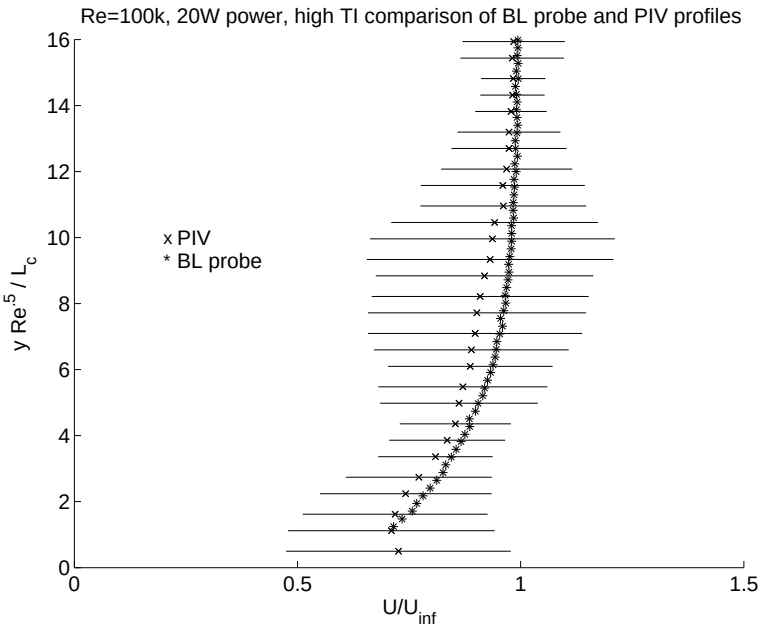

Figure B.12: Comparison of BL probe and PIV data, $Re \approx 100k$, high TI.

B.2 Velocity Profiles Normal to Electrode

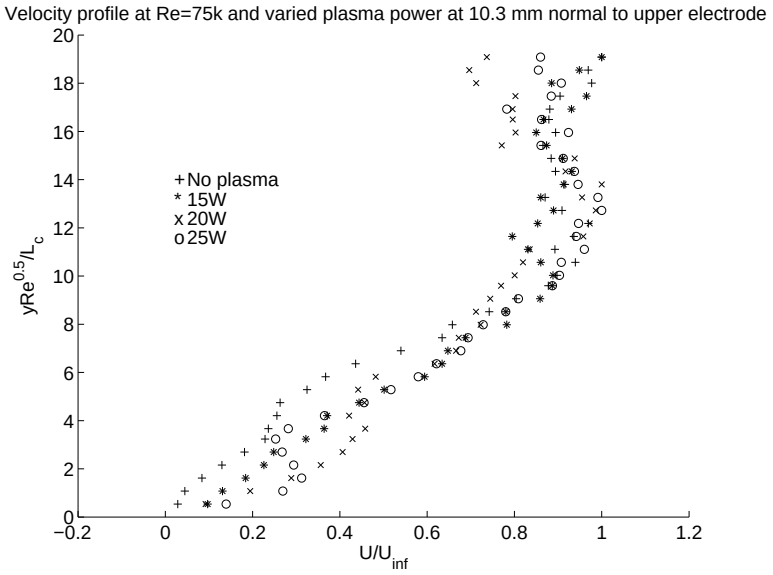

Figure B.13: Velocity profiles, $Re \approx 75k$, varied power levels, low TI.

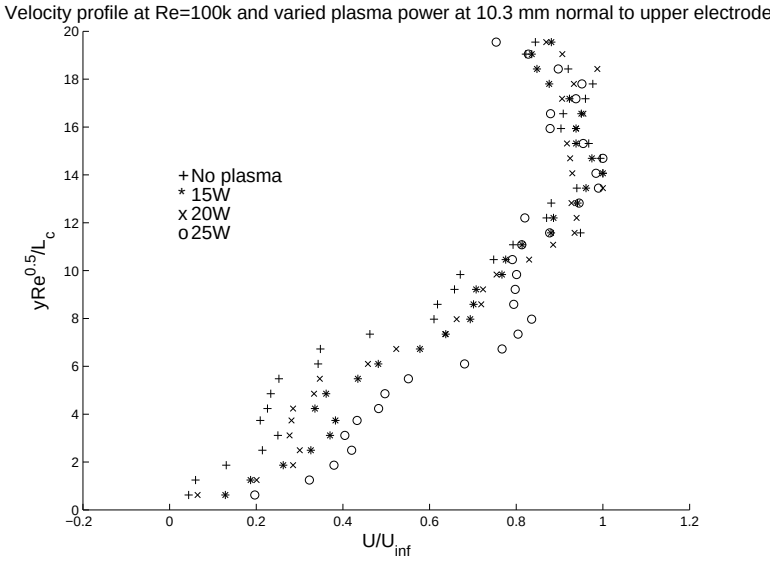

Figure B.14: Velocity profiles, $Re \approx 100k$, varied power levels, low TI.

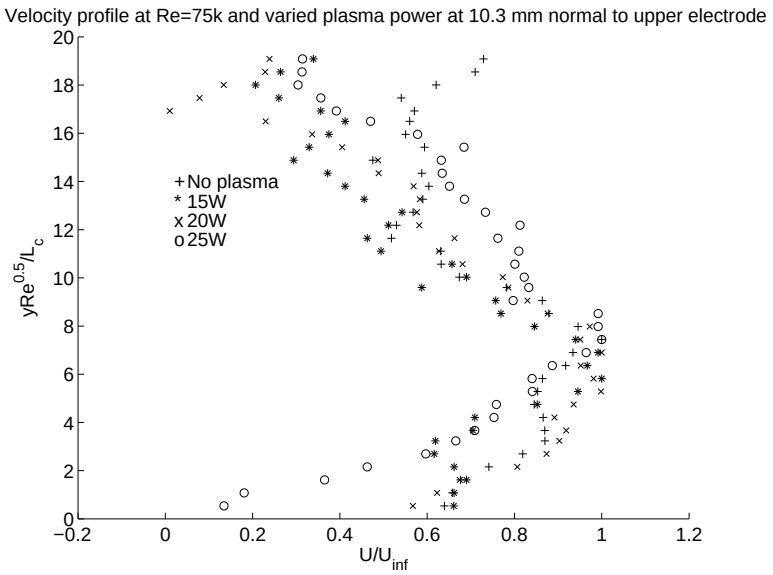

Figure B.15: Velocity profiles, $Re \approx 75k$, varied power levels, high TI.

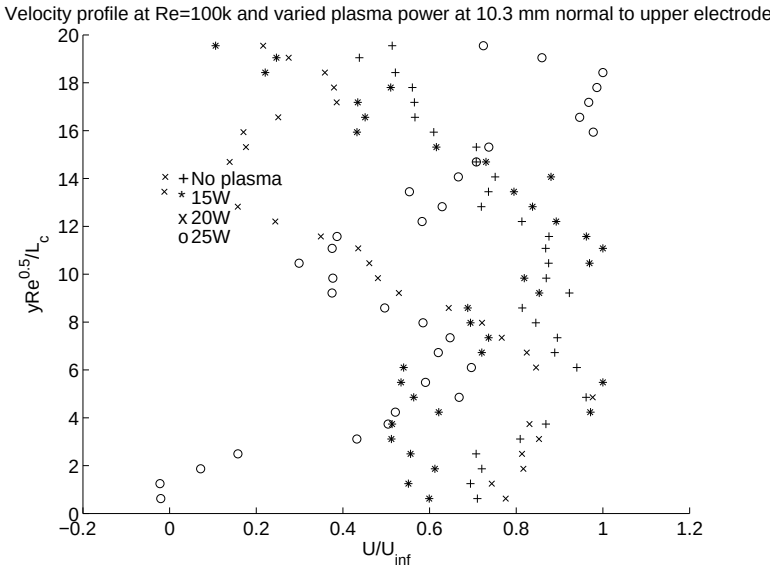

Figure B.16: Velocity profiles, $Re \approx 100k$, varied power levels, high TI.

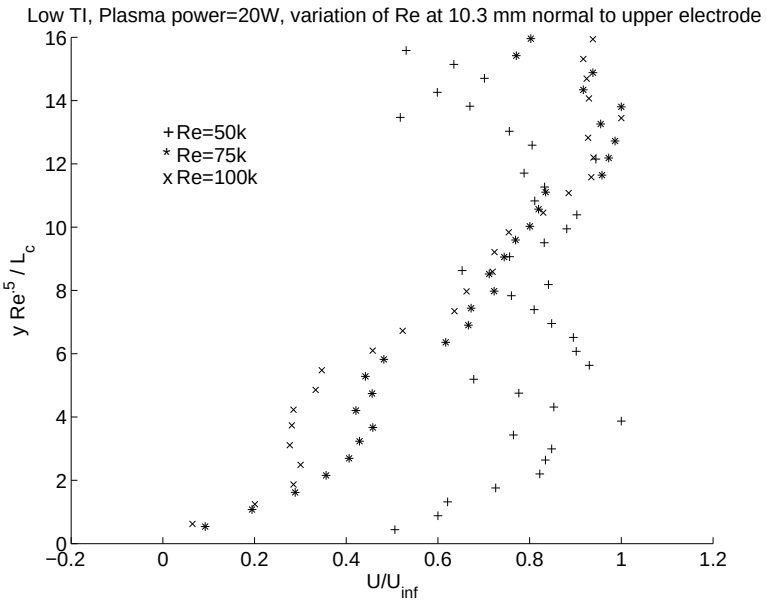

Figure B.17: Velocity profiles, 20W power, varied Re, low TI.

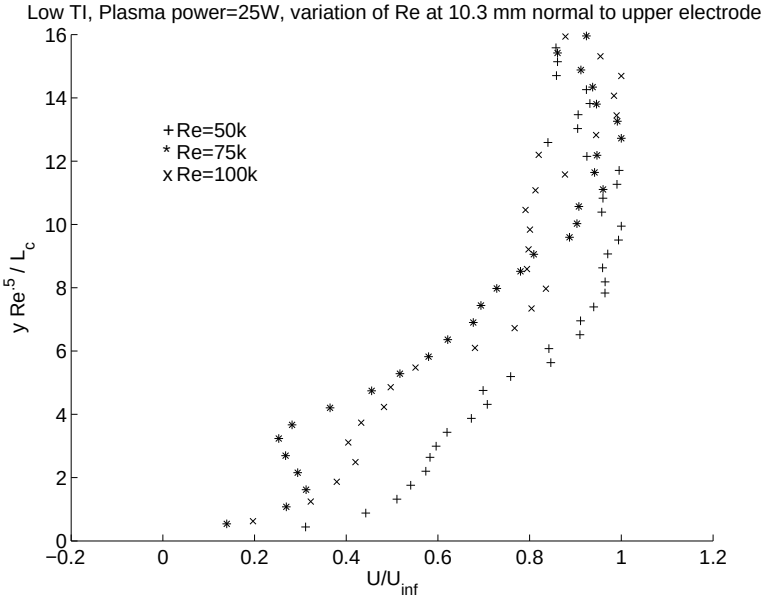

Figure B.18: Velocity profiles, 25W power, varied Re, low TI.

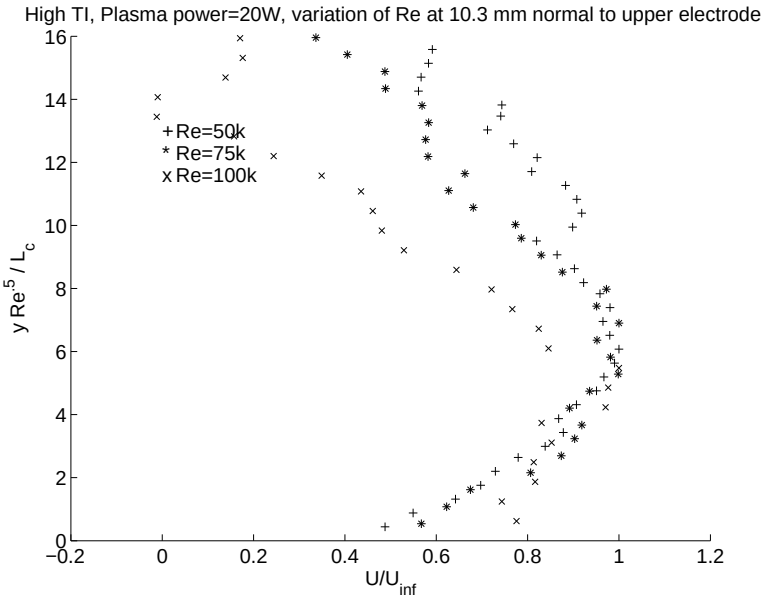

Figure B.19: Velocity profiles, 20W power, varied Re, high TI.

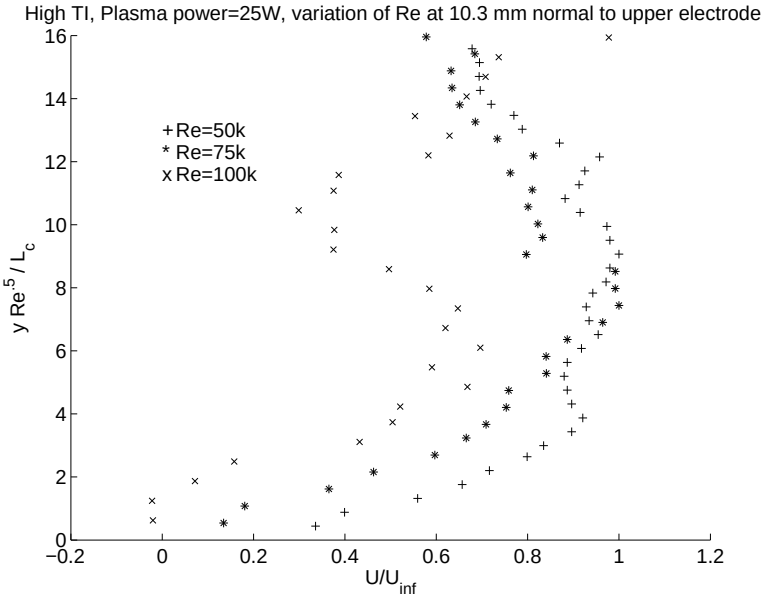

Figure B.20: Velocity profiles, 25W power, varied Re, high TI.

B.3 Momentum Thickness Reynolds Number Calculations

The momentum thickness θ was found using:

$$\theta = \Sigma_y \frac{u(y)}{U_{inf}} \left(1 - \frac{u(y)}{U_{inf}}\right), \tag{B.1}$$

where the sum was over every point of data collected. The sum over all points was equivalent to the integral from 0 to a point where the local velocity was essentially 99% of the free stream velocity. Re_θ was then found using the following equation:

$$Re_\theta = \frac{\rho U \theta}{\mu}, \tag{B.2}$$

where U was the free stream velocity, and the density, ρ, and viscosity, μ, were the values assigned for air at 860 ft above sea level.

The results of the Re_θ calculations for each data run are tabulated in table B.1.

Table B.1: Re_θ calculation results

Re_c	Power	TI	Re_θ
$5.0{\cdot}10^4$	15W	low	770
$7.5{\cdot}10^4$	15W	low	416
$10.0{\cdot}10^4$	15W	low	740
$5.0{\cdot}10^4$	20W	low	691
$7.5{\cdot}10^4$	20W	low	717
$10.0{\cdot}10^4$	20W	low	1019
$5.0{\cdot}10^4$	25W	low	593
$7.5{\cdot}10^4$	25W	low	574
$10.0{\cdot}10^4$	25W	low	-84
$5.0{\cdot}10^4$	15W	high	821
$7.5{\cdot}10^4$	15W	high	1045
$10.0{\cdot}10^4$	15W	high	1128
$5.0{\cdot}10^4$	20W	high	776
$7.5{\cdot}10^4$	20W	high	1002
$10.0{\cdot}10^4$	20W	high	1395
$5.0{\cdot}10^4$	25W	high	771
$7.5{\cdot}10^4$	25W	high	1113
$10.0{\cdot}10^4$	25W	high	1275

Appendix C. Plasma Characteristics

Each set of data was taken at a given voltage and frequency as selected on a HVPS. Voltage, current, and time data were outputted to a text file via National Instruments LabVIEW. The text file was then manipulated using MATLAB to produce voltage, current, and power plots. There were two sets of voltage and current data recorded via LabVIEW, one set corresponds to the upper electrode and the other corresponds to the lower electrode. The power was calculated using two separate formulae on a point by point basis, that is, at each time step calculated by LabVIEW. Note that the power was only computed with the values obtained from the upper electrode. In Section C.1, the voltage and current from each side of the transformer are plotted on the same plot, the left ordinate defines the values for voltage while the right ordinate defines the values for the current, in volts and amperes respectively. The abscissa displays the time in seconds. The power plots display the power calculated via Equations (2.4) and (2.3), again with respect to time in seconds.

C.1 Voltage and Current Plots

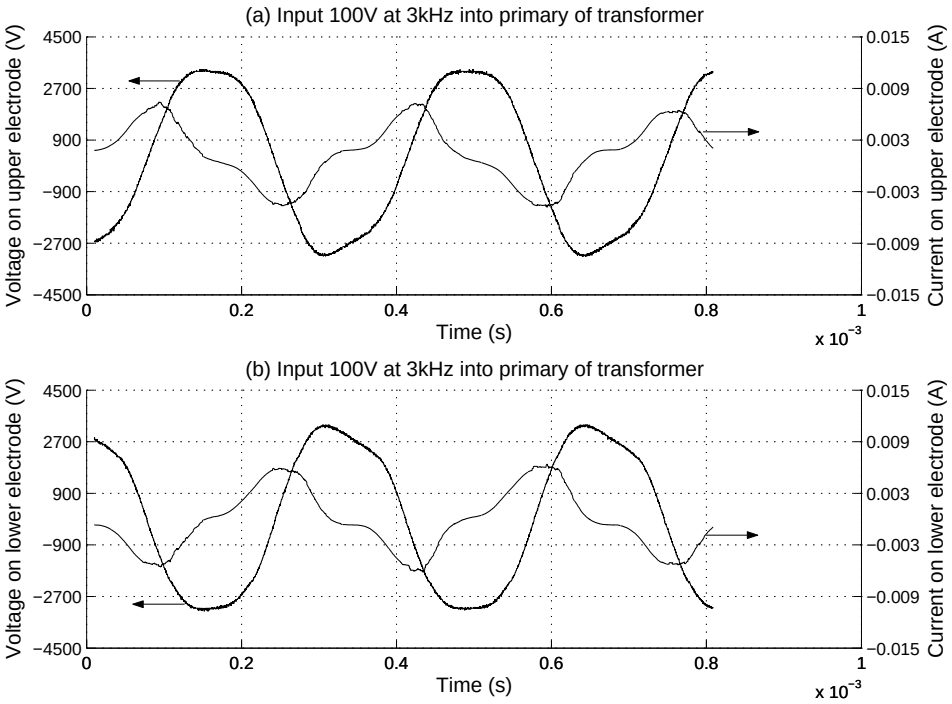

Figure C.1: Voltage and current on (a) upper and (b) lower electrodes, input 100V at $3kHz$.

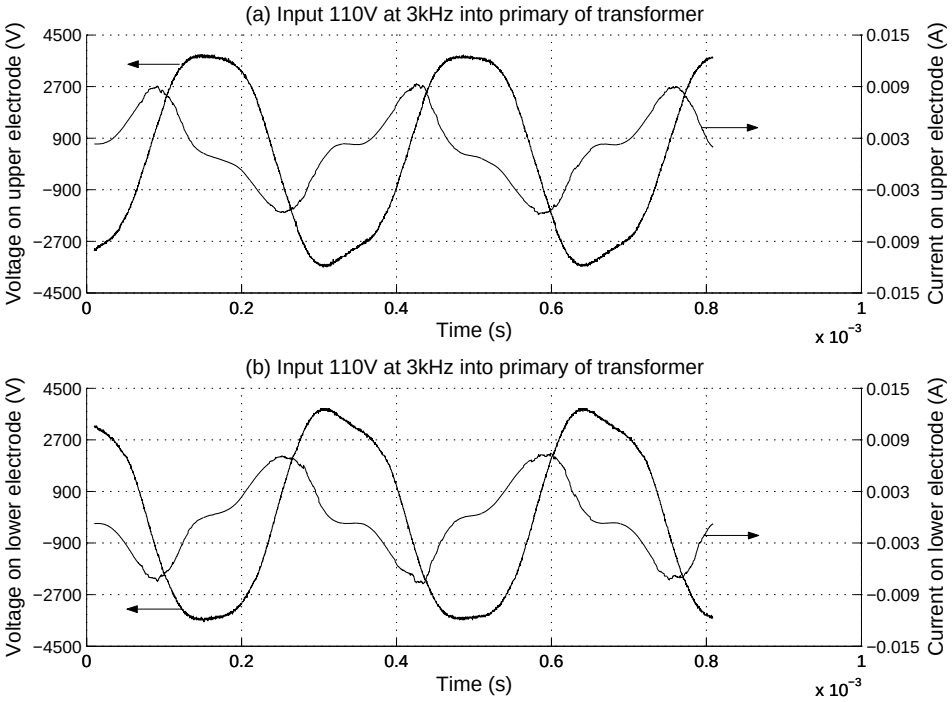

Figure C.2: Voltage and current on (a) upper and (b) lower electrodes, input 110V at $3kHz$.

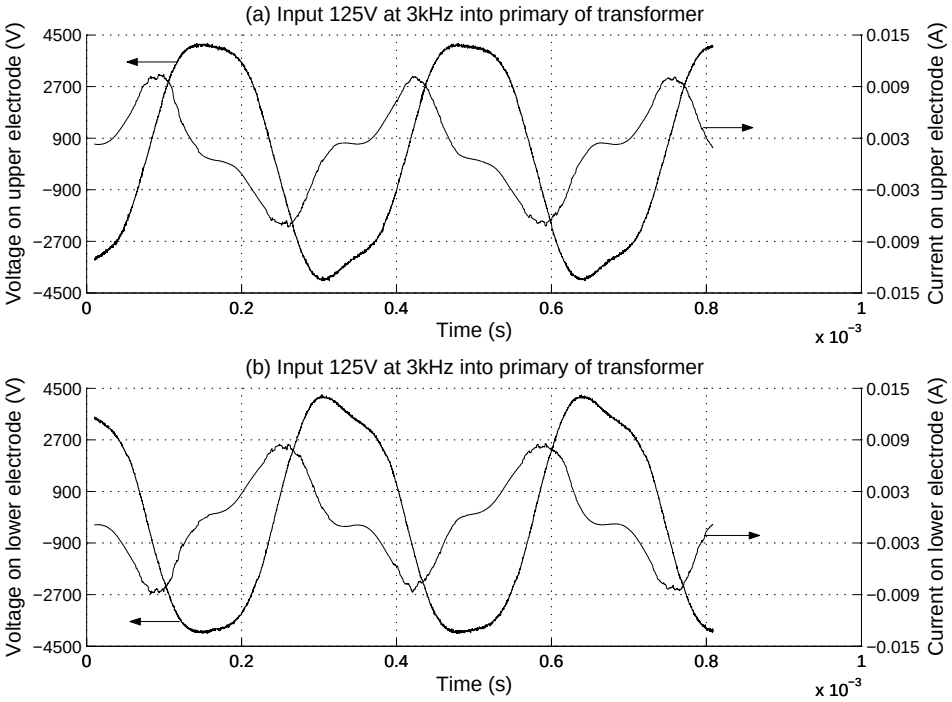

Figure C.3: Voltage and current on (a) upper and (b) lower electrodes, input 125V at $3kHz$.

C.2 Displayed versus Calculated Power Comparisons

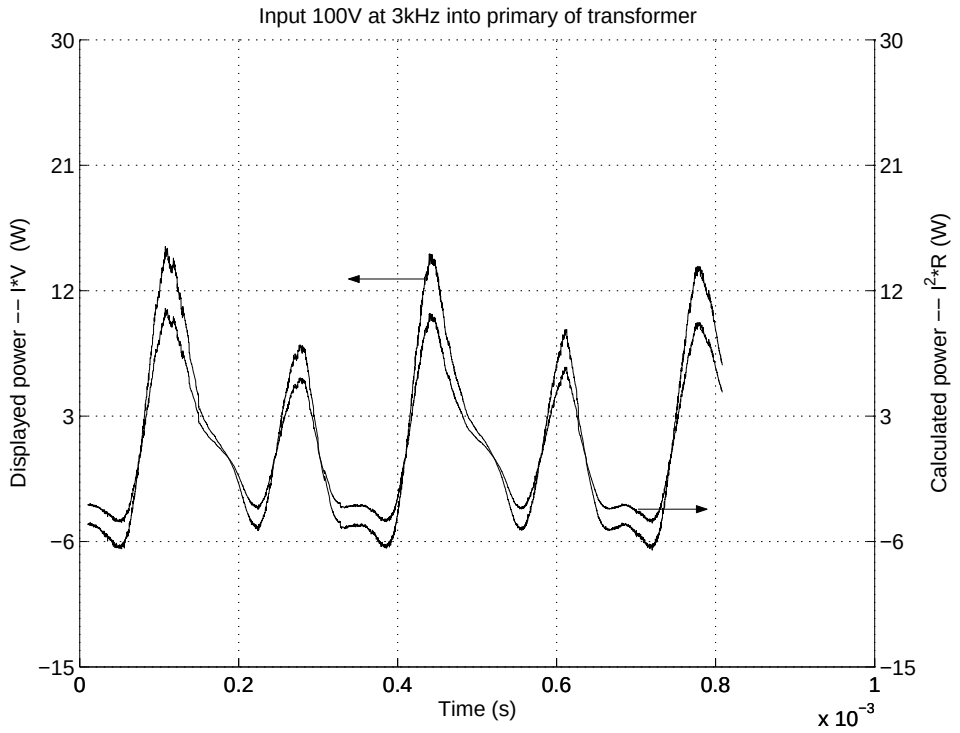

Figure C.4: Power levels, input 100V at $3kHz$.

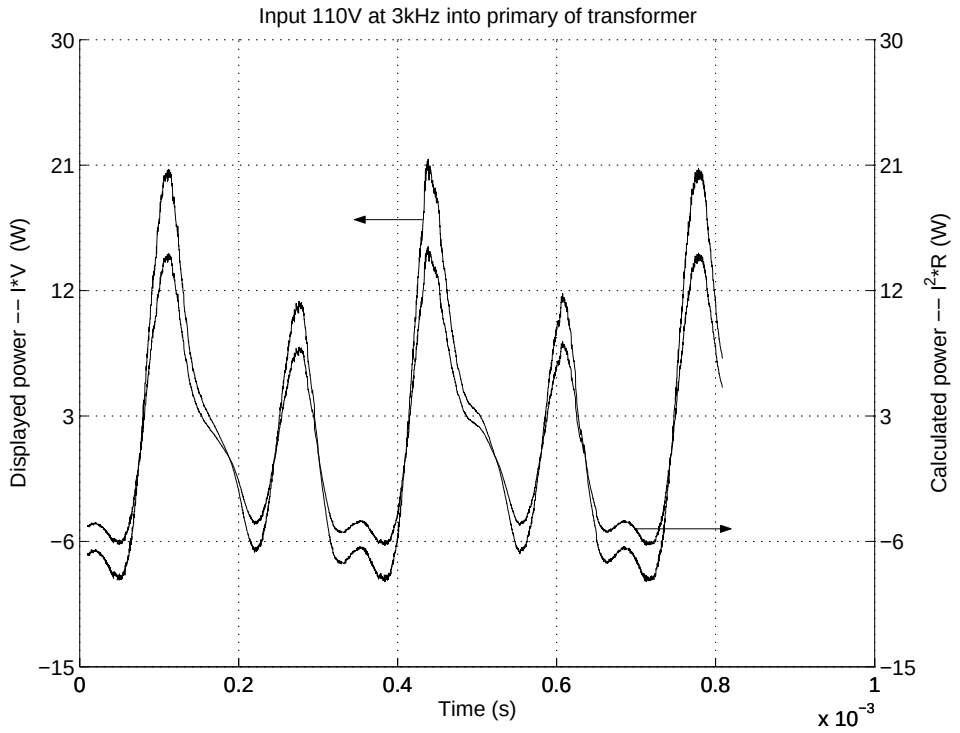

Figure C.5: Power levels, input 110V at $3kHz$.

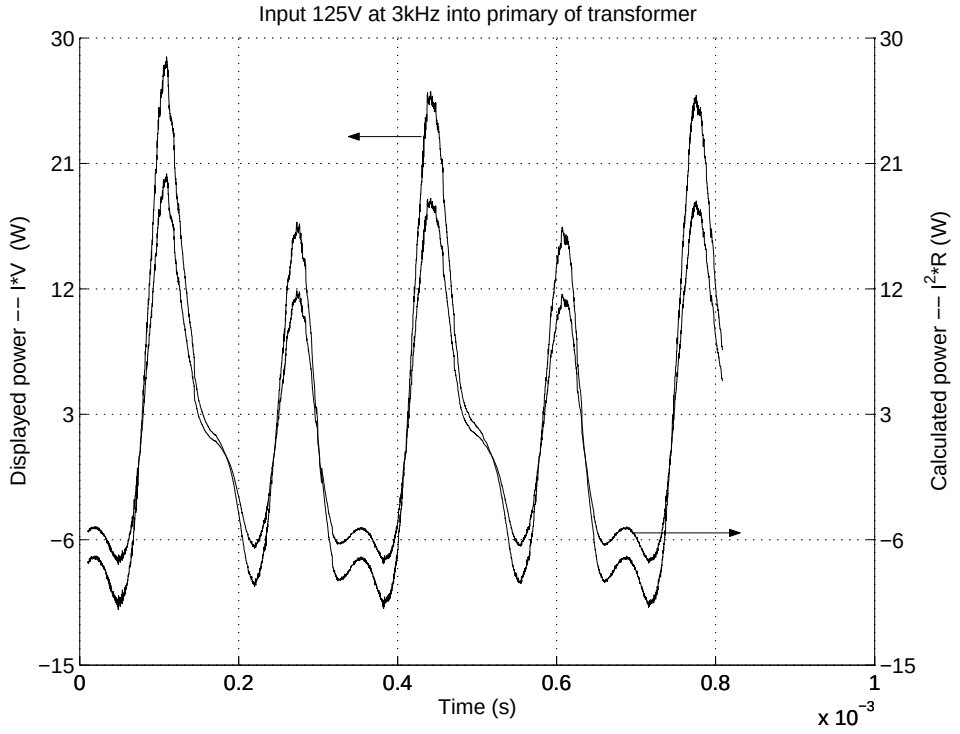

Figure C.6: Power levels, input 125V at $3kHz$.

Appendix D. Hot Film Calibration

D.1 Procedure For Calibration of Hot Film Anemometer

Begin by ensuring that you have TSI cables; Anemometer channel is set for proper cable length and sensor type; Anemometer is given sufficient time to stabilize temperature (30 min.).

Measuring Cable Resistance

1. Install the shorting plug in the end of the probe holder to be used during testing
2. Press RES MEAS to select the NULL DISPL mode.
3. Adjust the OPERATE RES knob to zero the display (balance the bridge)
   Note: The OPERATE RES knob is a continuous pot, there are two levels of resistance on the knob, the lesser resistance is for fine adjustment and the greater resistance is for course adjustment.
4. Press RES MEAS to select the DISPL RES mode. The measured cable resistance will be displayed - record this value.
5. Press ENTER to store the value of the cable reisistance in the IFA-100 memory.

Measuring Probe Resistance and Calculating the Overheat Ratio

1. Blow air through the calibration jet to remove any dirt particles.
2. Carefully install the probe to be calibrated in the probe holder. Tighten the probe holder into the probe holder traverse of the calibration jet so that the probe is less than one jet diameter ($\approx 0.25in$) from the exit of the jet, centered over, and normal to the flow.
3. With the pressure tap disconnected, verify the zero reading of the transducer using a virtual channel in NI Measurement and Automation. Connect the pressure tap from the calibration jet to the transducer.
4. Adjust the flow regulator on the calibration jet to $\approx 0.05inH_2O$.
5. Press RES MEAS to select the DISPL RES to display the measured probe resistance - record this value.
6. Calculate the operating resistance:
   OR = ((Probe Resistance - Internal Probe Resistance (R_{int}))$\cdot$ OHR) + R_{int},
   where OHR = 1.5 for a hot film probe and 1.8 for a hot wire probe.
7. Press OPERATE RES and adjust the OPERATE RES knob until the display value matches your calculated value.
8. Press ENTER to store this value.

Adjust the Bridge Frequency Compensation

1. Press BRIDGE COMP and adjust the BRIDGE knob until the displayed value matches the correct value where: BRIDGE COMP ≈ 115 for a film probe, ≈ 35 for a wire probe
2. Press ENTER to store the value.
3. Increase the calibration jet flow to the maximum expected flow while testing.
4. Press RUN/STANDBY to go to "RUN" mode.
5. Turn the CABLE knob fully CCW. If the OSC light is off, then go to step 7.
6. Turn the CABLE knob CW until the OSC light goes out. Go to step 8.
7. Turn the CABLE knob CW until the OSC light illuminates. Turn the CABLE knob CCW until the OSC light turns off. Frequency Compensation is roughly adjusted.
8. Connect the signal out to an oscilloscope to monitor the OUTPUT. Set the oscilloscope to $\approx 10\frac{mV}{div}, \approx 200\frac{\mu s}{div}$, and normal trigger.
9. Press TEST SIGNAL and adjust the CABLE knob until a desirable waveform without oscillations is visible on the oscilloscope.

Bibliography

1. Barlow J. B., Rae W. H., and Pope A. *Low Speed Wind Tunnel Testing, Third Edition*. New York: John Wiley & Sons, 1999.

2. Bons J., MacArthur C., and Rivir R. "The Effect of High Freestream Turbulence on Film Cooling Effectiveness," *Transactions of the ASME*, *ASME paper 94-GT-51* (1994).

3. Bradshaw P. *An Introduction to Turbulence and Its Measurement*. New York: Pergamon Press, 1971.

4. Cebeci T. and Smith A. M. O. *Analysis of Turbulent Boundary Layers*. New York: Academic Press, Inc., 1974.

5. Chen Z. "Impedance Matching for One Atmosphere Uniform Glow Discharge Plasma (OAUGDP) Reactors," *IEEE Transactions on Plasma Science*, *30, No. 5*:1922–1930 (October 2002).

6. Enloe C., McLaughlin T., VanDyken R., and Fischer J. "Plasma Structure in the Aerodynamic Plasma Actuator," *American Institute of Aeronautics and Astronautics*, *AIAA Paper 2004-0844* (2004).

7. Harper C. A. and Sampson R. N. *Electronic Materials and Processes Handbook*. New York: McGraw-Hill, Inc., 1994.

8. Hultgren L. and Ashpis D. "Demonstration of Separation Delay With Glow-Discharge Plasma Actuators," *NASA/TM-2003-212204* (2003).

9. Jacob J., Rivir R., Carter C., and Estevadeordal J. "Boundary Layer Flow Control Using AC Discharge Plasma Actuators," *American Institute of Aeronautics and Astronautics*, *AIAA Paper 2004-2128* (2004).

10. Kays W. and Crawford M. *Convective Heat and Mass Transfer*. New York: McGraw-Hill, Inc., 1980.

11. King L. V. "On The Convection of Heat from Small Cylinders in a Stream of Fluid: Determination of the Convection Constants of Small Platinum Wires with Applications to Hot-Wire Anemometry," *Philosophical Transactions of the Royal Society*, *A214*:373–432 (1914).

12. Kraus J. D. *Electromagnetics*. New York: McGraw-Hill, Inc., 1953.

13. Liberzin A., Gurka R., and Hetsroni G. "Vorticity Characterization in a Turbulent Boundary Layer Using PIV and POD Analysis." *4th International Symposium on Particle Image Velocimetry*. September 2001.

14. "Radiation Dose Chart", *American Nuclear Society*, January 2005. http://www.ans.org/pi/resources/dosechart/.

15. Rivir R., White A., Carter C., Ganguly B., Jacob J., Forlines A., and Crafton J. "AC and Pulsed Plasma Flow Control," *American Institute of Aeronautics and Astronautics*, *AIAA Paper 2004-847* (2004).

16. Roach P. E. "The Generation of Nearly Isotropic Turbulence by Means of Grids," *Heat and Fluid Flow*, *8, No. 2*:82–92 (June 1987).

17. Roth J., Sherman D., and Wilkenson S. "Bondary Layer Flow Control With a One Atmosphere Uniform Glow Discharge Plasma," *American Institute of Aeronautics and Astronautics*, *AIAA Paper 98-0328* (1998).

18. Roth J., Sherman D., and Wilkenson S. "Electrohydrodynamic Flow Controd with a Glow-Discharge Surface Plasma," *American Institute of Aeronautics and Astronautics*, *38, No. 7*:1166–1172 (July 2000).

19. Schlichting H. and Gersten K. *Boundary Layer Theory, Eight Revised and Enlarged Edition*. India: Springer, 2001.

20. VanDyken R., McLaughlin T., and Enloe C. "Parametric Investigations of a Single Dielectric Barrier Plasma Actuator," *American Institute of Aeronautics and Astronautics*, *AIAA Paper 2004-0846* (2004).

21. Volino R. J. and Hultgren L. S. "Measurements in Separated and Transitional Boundary Layers Under Low-Pressure Turbine Airfoil Conditions," *Journal of Turbomachinery*, *123*:189–197 (April 2001).

22. Wheeler A. J. and Ganji A. R. *Introduction To Engineering Experimentation*. Upper Saddle River, NJ: Prentice Hall, Inc., 1996.

23. Wilkenson S. P. "Investigation of an Oscillating Surface Plasma for Turbulent Drag Reduction," *American Institute of Aeronautics and Astronautics*, *AIAA Paper 2003-1023* (2003).

24. Wilson D. G. and Korakianitis T. *The Design of High-Efficiency Turbomachinery and Gas Turbines, Second Edition*. Upper Saddle River, NJ: Prentice Hall, Inc., 1998.

REPORT DOCUMENTATION PAGE

Form Approved
OMB No. 074-0188

PLEASE DO NOT RETURN YOUR FORM TO THE ABOVE ADDRESS.

1. REPORT DATE *(DD-MM-YYYY)*	**2. REPORT TYPE**	**3. DATES COVERED** *(From – To)*
22-03-2005	**Master's Thesis**	Aug 2004 – Mar 2005

4. TITLE AND SUBTITLE

BOUNDARY LAYER FLOW CONTROL USING PLASMA INDUCED VELOCITY.

5a. CONTRACT NUMBER

5b. GRANT NUMBER

5c. PROGRAM ELEMENT NUMBER

6. AUTHOR(S)

Balcer, Brian E., 2Lt, USAF

5d. PROJECT NUMBER

5e. TASK NUMBER

5f. WORK UNIT NUMBER

7. PERFORMING ORGANIZATION NAMES(S) AND ADDRESS(S)
Air Force Institute of Technology
Graduate School of Engineering and Management (AFIT/EN)
2950 Hobson Way
WPAFB, OH 45433-7765

8. PERFORMING ORGANIZATION REPORT NUMBER

AFIT/GAE/ENY/05-M03

9. SPONSORING/MONITORING AGENCY NAME(S) AND ADDRESS(ES)
AFRL/PR
Attn: Dr. Richard B. Rivir
1950 5th Street
WPAFB, OH 45433-7521 DSN: 785-2744

10. SPONSOR/MONITOR'S ACRONYM(S)

11. SPONSOR/MONITOR'S REPORT NUMBER(S)

12. DISTRIBUTION/AVAILABILITY STATEMENT
APPROVED FOR PUBLIC RELEASE; DISTRIBUTION UNLIMITED.

13. SUPPLEMENTARY NOTES

14. ABSTRACT

An examination of the effects of plasma induced velocity on boundary layer flow was conducted. A pair of thin copper film electrodes spanned the test section, oriented at thirty degrees from normal to the free stream flow. An adverse pressure gradient was imposed over the electrode configuration using a pressure coefficient profile similar to that associated with suction side of a Pac-B low pressure turbine blade. In addition, suction was applied to keep flow attached on the upper wall, inducing separation over the electrode. The electrode is supplied by an AC source at three different power levels with the free stream flow at three separate chord Reynolds numbers. The chord length was based on the geometry of the simulated airfoil profile used for the upper wall of the test section. The flow turbulence intensity was varied by means of a passive grid in the upstream flow. Velocity data were collected using particle imaging velocimetry as well as with a boundary layer pitot probe. The power levels applied to the plasma were between 20 and 40 watts. The flow regimes studied were between chord Reynolds numbers of 50,000 to 100,000. It was found that the use of plasma to control the boundary layer enabled the flow to remain attached in the presence of an adverse pressure gradient. However, at the studied Reynolds numbers and electrode configuration the plasma was unable to affect an already separated flow regardless of the power input to the electrode. It was finally ascertained that two types of turbulent structures could be resolved, one being a counter-rotating vorticity pair and the other being a counter-rotating vorticity sheet.

15. SUBJECT TERMS
Plasma Discharge, Dielectric Barrier Discharge, Particle Imaging Velocimetry, Turbulence, Photofabrication,

16. SECURITY CLASSIFICATION OF:			**17. LIMITATION OF ABSTRACT**	**18. NUMBER OF PAGES**	**19a. NAME OF RESPONSIBLE PERSON**
REPORT	**ABSTRACT**	**c. THIS PAGE**			Milton B. Franke, PhD, AFIT/ENY
U	**U**	**U**	**UU**	113	**19b. TELEPHONE NUMBER** *(Include area code)* (937) 255-3636, ext 4720